angeo-2018-90 reply to referees
In this revised version, we have tried to respond to the referees' constructive suggestions.

angeo-2018-90-RC1:

Line 185: "correctness of the break point"
The analysis is insensitive to the precise value for the breakpoint and for the events we found, the populations are quite distinct so any additional precision would add anything significant. Also, it is perhaps worth pointing out that the events shown in this paper are the only ones that we were able to find—foreshock events in burst mode data are not very numerous.

Sections 4.2 and 4.3: authors just refer to other papers for the shock normal determination method and for the energization method. Since these techniques are extensively used in the analysis, I recommend to describe them with more detail.

Reviewing the method described in Paschmann 1980 would require a lengthy and complicated insertion that would merely reproduce elements of the 1980 paper. The technique is not particularly new, so we feel that the interested reader can glean the necessary details directly from the referenced paper.

Regarding the estimation of the pitch angle spread, what is the time window over which you compute the average magnetic field?
4 sec, i.e., one spin.

The text around line 415 has been rewritten.

Figure 2: Please delete from the header 'Full, Strahl'. In the caption change '0.09 eV' with '0.09 cmˆ(-3)'.
Fixed

Please discuss in Section 5.4 how all the sources of errors can influence the main.
The errors in the analysis are primarily statistical and the conclusions will not be substantially affected by those errors. More events would, of course, help, but there are no more events in the Cluster data. Perhaps future analyses using data from MMS will provide more insights.

Line 423: please add here references to simulations, as the already quoted.
Done

In this revised version we have tried to address the referee's concerns:

1/ … the performed analysis, the conclusions about the location of reflection are rather too strong and should be better presented as a possible hypothesis which proof will definitely require some additional analysis …

We have changed the title of the paper and modified the discussion and conclusions. It is perhaps worth reiterating that this analysis was carried out on all the available burst mode data. To expand the analysis in the future, one would have to use data from, for example, the MMS mission. Whether a useful population of foreshock events can be found in MMS data is a subject for future study.

*3/ A substantial part of the whole analysis is based on many "subjective" threshold values…*

We have tried to be a quantitative as possible given the observational constraints. We feel that the examples are compelling. Regardless of the fine points, it is nonetheless clear that from these examples and from the phi-theta plots that the reflection of the strahl is not coincident with any increase in the magnitude of the magnetic field and, consequently, there is no evidence that magnetic mirroring is playing an important role in the reflection. To be more quantitative would require more examples, which are, unfortunately, not available.

4/ For the complete picture it could be of interest to plot not only the variation of the B-field magnitude (Figure 14) but also of the individual components to see how the magnetic background is stable or not. This is highly relevant namely when discussing the B angle to the shock normal.

We attach a plot of the components, but since the plot does not add any information other than confirming that the computed shock normal is a good estimation of the geometry of the event, we have chosen not to include it in the paper. Should the referee disagree, we would be happy to include it, but, frankly, don't think that it would add anything significant to the analysis.

In this plot, the data have been rotated into the shock normal coordinate system and the B_dot_n component is continuous across the shock in the rotated system (rotated Bx), indicating a relative good normal calculation.

CLUSTER-2/FGM Magnetic Field Data 5VPS
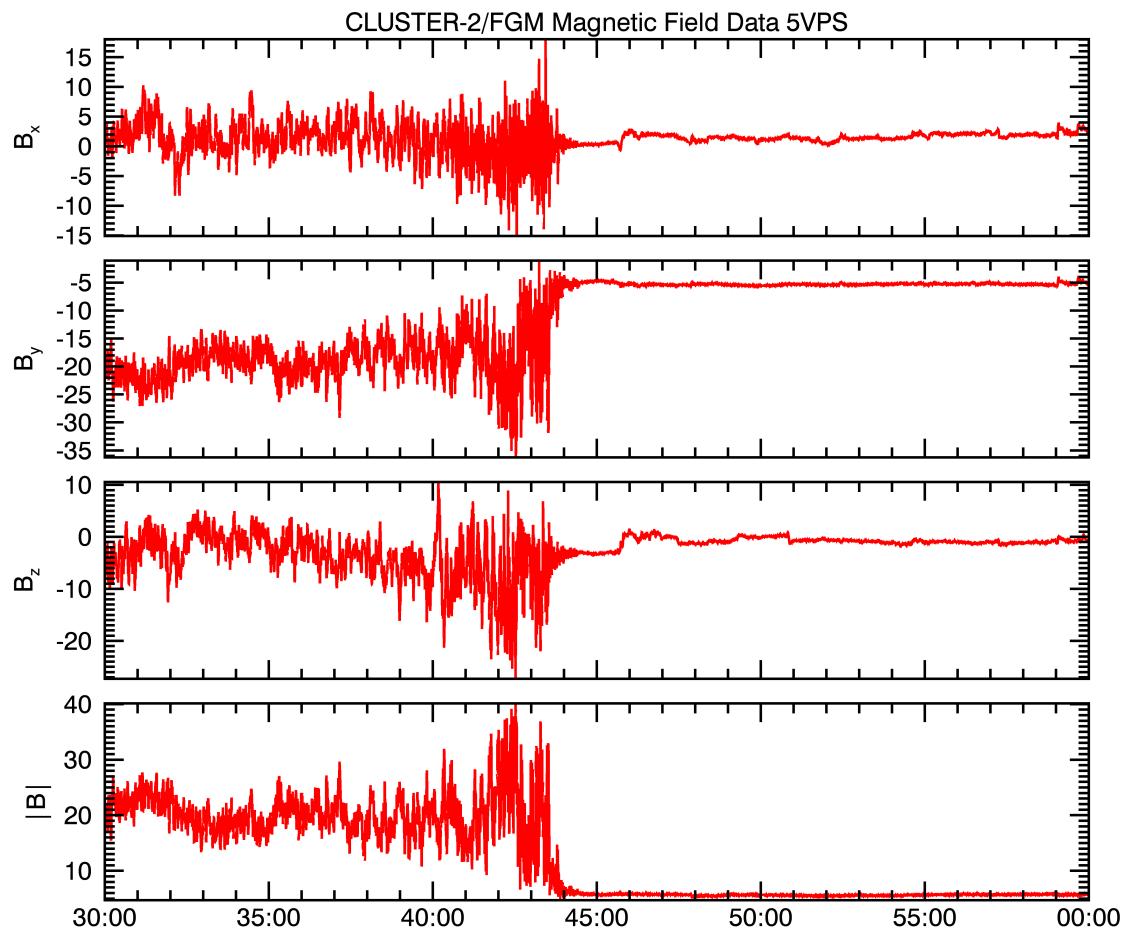
5/ (and /6) The PT plots should display some color bar to give information about the scale of the color maps. In the present form it is impossible to see what is the level of variation and how the strahl/reflected electrons are significant wrt to the core-halo part….

The color bars are normalized for each energy. The variation with energy is too large to use a uniform color bar for each event. Consequently, in this usage, the "PDF" does not sum to unity.

7/ When plotting the NR/NS ratio, consider adding a line y=1 so the reader can better see what is the variation around the "total" reflection. Also the y-scale on Figure 13 for this ratio can be adjusted accordingly, here the max value is too high

Unfortunately, these plot were made using software created by the (deceased) first author and we do not have access to the scripts that generated the plots. Consequently, although we agree that it would be useful to make the changes suggested, we are unable to do so.

line 65 - It is often... a verb is missing?

Fixed.

line 74 - remove "it" after mirroring

Fixed.

line 76 - though -> through

Corrected.

line 129 - What is UDF Analysis, it is generally known or should be describd here (or removed)

That analysis package has been used in previous publications; we have removed the reference.

line 178 - (also related to comment 3/) high/low density wrt what? What about to consider normalizing the NR by NT? Would it make the foreshock determination more robust?

We think that the description is clear and, for the reasons mentioned above, cannot easily change the normalization, nor do we think that doing so would substantially change the determination of the foreshock.

line 212 - What is QGM? Either remove or explain a bit.

We've removed QGM.

line 303 - The meaning of the last sentence is not clear even from the context.

We don't know what is unclear here.

line 308-309 - Would the return population "become more gyrotropic" (full ring) when plotting the PT plot in the solar wind frame?

Since the electron speeds are much greater than Vsw, changing the reference frame of the plot (again, not easily doable), should not make any significant difference.

line 387 - remove "eV", the energization factor has no units

Fixed.

line 408 - effect -> affect?

Fixed

line 526 - are -> is

Fixed.

line 533-539 - This paragraph should be placed later in the Conclusions. First one should recall the MAIN results.

We have done that and slightly reworded the conclusions.

~~Total~~ Reflection of the Strahl within the Foot of the Earth's Bow Shock

Christopher A. Gurgiolo[*1], Melvyn L. Goldstein[2], and Adolfo Viñas[3]

[1]Bitterroot Basic Research, Hamilton, MT, USA
[2]Space Science Institute, Boulder, CO, USA
[3]Department of Physics, American University, Washington, DC 20016, USA, and Geospace Physics Laboratory, NASA Goddard Space Flight Center, Greenbelt, MD, USA

Correspondence to: Melvyn L. Goldstein
(u2mlg1@gmail.com)

[*]Deceased

Abstract. The reflection of a fraction of the solar wind at the bow shock to some extent defines the physical properties of what is known as the foreshock, the region where the interplanetary magnetic field has a direct connection to the bow shock. Both ion and electron reflection have been observed and together form a significant source of free energy that is responsible for many of the instabilities

5 observed in this region. In this paper we concentrate on reflection of electrons at the shock and report two significant findings: The first is that the strahl, the field aligned component of the electron solar wind distribution, appears to be~~is~~ fully reflected at the bow shock; the second finding is that the reflection is observed to occur~~s~~ in the foot of the shock and not in the shock ramp. Thi~~se~~ latter observation implies that mirroring ~~appears~~in these examples~~n~~is not ~~to~~the primary determinant of

10 ~~play, at most, only a minor role in~~ the electron reflection process.

1 Introduction

The region upstream of a planetary bow shock that is magnetically connected to the shock is known as the foreshock (Russell et al., 1971). This is a highly dynamic and often turbulent region characterized not only by a solar wind presence but also by the presence of ion and electron distributions

15 formed from solar wind particles reflecting at the shock and propagating back into the upstream solar wind along the magnetic field (Paschmann et al., 1981; Thomsen et al., 1983; Gedalin, 2016). These latter distributions may also include particles that have leaked back upstream from downstream of the shock (Gosling et al., 1989). We will not distinguish these distributions, and will, for convenience, label them simply as *return* distributions.

20   Although partial reflection of both solar wind ions and electrons off Earth's bow shock has been recognized for many years (Gosling et al., 1978; Bonifazi and Moreno, 1981a,b; Anderson et al., 1985; Gosling et al., 1989) most studies have focused on ion observations because:

1. The solar wind ion velocity distribution function (VDF) is generally less complex than that of the electrons, despite the fact that the ion distributions do vary with solar activity when fast
25   streams may contain field aligned beams and heavier ions, such as Helium. On the other hand, the electron VDF are generally far from Maxwellian in shape and typically consists of three component populations; core, halo, and strahl that together can extend from a few eV into the keV range.

2. The ions have substantially longer gyro-periods, which allows for detailed studies of the evo-
30   lution of the post reflection VDFs by typical electrostatic analyzers that often require seconds to acquire a full 3D VDF.

3. The solar wind ions, being of much higher energy than the electrons, are less susceptible to issues that often plague measurements of the solar wind electrons, such as spacecraft charging, low energy photo-electrons, noise, etc.

35   It has generally been assumed that results obtained from the ion studies are also applicable to the reflection of electrons from the shock, but this assumption has not been intensively investigated.

    At least for ions, the specifics of the reflection of the solar wind at the bow shock are dependent, to some degree, on whether the reflection occurs in a quasi-parallel or quasi-perpendicular shock configuration (see eg., Fuselier and Schmidt, 1994). In specular reflection off a quasi-perpendicular
40   portion of a shock, the guiding center of the reflected particle is directed downstream often allowing for multiple reflections off the shock and the reflection efficiency can reach as high as 20% of the incident solar wind (Paschmann and Sckopke, 1983). Reflections off a quasi-parallel shock show a much lower reflection efficiency and result in a guiding center motion which is predominantly directed upstream (Gosling et al., 1982; Schwartz and Marsch, 1983). Yuan et al. (2007), using sim-
45   ulations have shown electron reflection percentages as high as 10%, the percentage being dependent on the size of the shock magnetic field overshoot.

    Return distributions are almost always field-aligned and are often non-gyrotropic for both electrons and ions. The anisotropy basically is the result of gyrophase-bunching that can occur in the reflection process (Gurgiolo et al., 1983) and is integral to the formation of the partial and full
50   ring distributions observed in the foreshock. Those distributions are thought to be derived from the phase-mixing of initially gyro-phase bunched distributions as they propagate away from the shock (Gurgiolo et al., 1993; Mesiane et al., 2001; Meziane et al., 2004). Often, as seen in simulations of ion reflection off the shock, the gyro-phase mixing is arrested early in the distribution's propagation upstream when the rotating gyro-phase bunched particles begin to drive large-scale MHD waves that

themselves trap the distribution, locking it in phase (Thomsen, 1985; Gurgiolo et al., 1993). Phase-locked electrons have been observed well upstream of the shock in the presence of whistler waves (Gurgiolo et al., 2005). The process is generally used to explain observations of phase-bunched distributions made at distances upstream of the shock beyond where gyro-phase mixing should have led to isotropization.

Return distributions contain sufficient free energy to drive a number of instabilities commonly observed in the foreshock. These include observations of MHD and ULF waves (Hoppe et al., 1981; Greenstadt et al., 1995), ion and electron cyclotron waves (Smith et al., 1985; Kis et al., 2007), whistler waves (Hoppe and Russell, 1980; Zhang et al., 1998), ion acoustic waves (Gurnett and Frank, 1978), and Langmuir waves (Bale et al., 1997). Many of these are important in the pre-heating and breaking of the solar wind prior to its interaction with the shock.

Simulations have been very useful in exploring those processes that are thought to act in the reflection and acceleration of the solar wind (e.g., gradient drift at the shock (Leroy et al., 1981; Krauss-Varban and Wu, 1989; Leroy et al., 1982; Scholer and Terasawa, 1990)). Direct observations of post reflected distributions are a second source (Burgess, 1987; Kucharek et al., 2004). There are few, if any, direct observations of the actual reflection process, which would be extremely useful in helping to identify the mechanisms responsible. There are probably multiple mechanisms that are active, either singularly or in concert, in the reflection process (Fitzenreiter et al., 1996; Yuan et al., 2007; Savoini et al., 2010). One of the most commonly invoked mechanisms is reflection through magnetic mirroring (Burgess and Schwartz, 1984; Leroy and Mangeney, 1984; Burgess, 1987), which occurs as the solar wind approaches the stronger shock magnetic field. However, as we will demonstrate below, magnetic mirroring does not appear to play a major role in the reflection of the strahl. Mirror-reflected distributions are distinctive and can easily be identified and readily differentiated from return particles that have leaked through the shock from the magnetosheath (Larson et al., 1996).

Almost all reflected particles undergo energization in the reflection process. This occurs in the repartition of the incident particle's parallel and perpendicular velocity with respect to the magnetic field in the reflection process. The energization is driven by changes in the perpendicular velocity that shifts the particles guiding center position with respect to the VxB electric field (Sonnerup, 1969; Paschmann et al., 1981). Under certain conditions, reflections can also act to decelerate the particle (de-energization).

In this paper we closely examine the reflection of solar wind electrons off the shock. In particular, we are interested in what portion of the solar wind is being reflected and where the reflection occurs. We will also demonstrate a very simple and novel method for determining when a spacecraft is inside the foreshock that we developed in conjunction with this study. The method does not require knowledge of the shock location, any knowledge of the parameters associated with the shock, nor any modeling.

2 Data

The data used in this study were provided by a number of experiments on-board the Cluster space-craft. These include: the **P**lasma **E**lectron **A**nd **C**urrent **E**xperiment (PEACE) (Johnstone et al., 1997; Fazakerley et al., 2010), the **Flux**gate **M**agnetometer (FGM) (Balogh et al., 1997; Gloag et al., 2010), the **E**lectric **F**ield and **W**aves (EFW) experiment (Gustafsson et al., 1997; Khotyaintsev et al., 2010), and the **W**aves of **Hi**gh frequency and **S**ounder for **P**robing of **E**lectron density by **R**elaxation (WHISPER) (Décréau et al., 1997; Trotignon et al., 2010).

The primary data used in this analysis are from PEACE, which consists of two hemispherical electrostatic analyzers designated HEEA (High Energy Electrostatic Analyzer) and LEEA (Low Energy Electrostatic Analyzer). They are located $180°$ apart on the satellite. The analyzers differ only in their geometric factors (HEEA's geometric factor is the larger one). Despite their acronyms, both can cover identical energy ranges from 0.6 eV to 26 keV. The analyzers' fields of view are perpendicular to the spacecraft spin axis, which is about $5°$ off GSE-Z and cover $180°$ in elevation in 12 sectors. A full $360°$ in azimuth is covered in one rotation of the spacecraft so that a three-dimensional snapshot of the electron distribution is accumulated once per spin ($\sim$4s).

Because of telemetry restrictions PEACE generally returns only a subset of the total data collected, even in burst-mode. Exactly what is returned depends on the instrument mode, which can be separately commanded for each analyzer on each of the four spacecraft. The telemetry rate, as well as the amount of data being returned, determines the time cadence at which full three-dimensional distributions are downloaded. During the time intervals used in this paper, all satellites were operating in burst-mode telemetry and PEACE was returning one 3D distribution per spin. Each distribution consisted of 30 energy bins with each bin divided into 6 or 12 elevations and 32 azimuths. In general, the C2 and C4 experiments returned 12 elevation bins while C1 and C3 returned only 6. Priority was given to using data from either C2 or C4 as the higher polar resolution greatly improved the registration of the strahl with respect to the magnetic field.

PEACE data are used to characterize the electron plasma using both moments and visualization tools that allow one to highlight aspects of the morphology in velocity space of the electron 3D Velocity Distribution Function (eVDF). Depending on the lower energy threshold coupled with the spacecraft potential there are times when the lower energy portion of the core electron population cannot be sampled. The FGM 5 vector per second data are used both to characterize the local magnetic field and to compute the shock normal. Both the EFW and WHISPER are used in the calculation of the electron moments; EFW provides the spacecraft potential used to correct the measured electron energy and WHISPER provides the flags necessary to filter out times during which the computed moments may be contaminated by local perturbations created by WHISPER active sounding.

All of the data used in the analysis presented in this paper were obtained from either of two open data archives: the Cluster Science Archive (CSA) (https://csa.esac.esa.int/csa-web/) and the Mullard

4

Space Science Laboratory (MSSL) Cluster Archive (http://www.mssl.ucl.ac.uk/missions/cluster/about_peace_data.php).

130   The CSA provides data in either CDF or CEF format; the MSSL archive returns data in IDFS format, which our analysis tools have been designed to handle.

3 $\phi - \theta$ Plots and Moments

A majority of the supporting analysis and conclusions in this paper come from either estimates of the plasma moments of the individual electron populations or from various features observed in
135   the $\phi - \theta$ plots (also referred to in the literature as "sky maps"). The $\phi - \theta$ plots are a good plot format for investigating three-dimensional features in eVDFs. For a full description, see Gurgiolo et al. (2010). A detailed description of how the moments are computed as well as how to separate electron populations within an eVDF can be found in Gurgiolo and Goldstein (2016). In the analysis presented here we use a slightly modified version of the population isolation method described in
140   the aforementioned paper. This is briefly outlined below.

Figure 1 contains 3 columns of $\phi - \theta$ plots illustrating the method used to separate the strahl and return electron populations. Only a subset of the returned energy steps are shown and each column of plots shows the same eVDF but with different masks applied. The same subset of the returned energy steps are displayed in each column. The first column has no mask applied and shows the
145   complete $\phi - \theta$ content within each of the plotted energy ranges. The black and red traces are lines of constant pitch-angle of $120°$ and $80°$, respectively. The second column of plots masks out all data with pitch-angles greater than $80°$ at energies $\geqq 47.9$ eV, which leaves just the return electrons. The third column masks out all pitch-angles less than $120°$ at energies $\geqq 56.7$ eV, which leaves only the strahl electrons.

150   The areas outside the masks have been set to zero so that the standard numerical integration technique used to estimate the basic plasma moments can be made over each of the three columns without any modifications. This approach yields the estimated plasma parameters associated with the full, return and strahl electron populations separately. The energy integrations for the latter two populations start at 47.6 and 56.7 eV respectively. Deciding the lower energy limit at which to begin
155   masking the data and over which the numerical integration is made is subjective and can ~~be~~ differ~~ent~~ for different populations. In general, we use the energy step above the first unambiguous observation of the population and should it overlap another population (as is often the case with the strahl and core-halo populations) the energy at which it becomes dominant. This energy is used for an entire event unless there is a clear indication that it has shifted up or down, in which case the moment
160   computations are terminated and restarted at the new time with the updated start energy.

4 Analysis Techniques, Terminology, Common Figure Formats

This section contains descriptions of the techniques used in the event analysis as well as terminology that may be unfamiliar and the plot formats used in some common figures. Presenting them separately allows them to be introduced in subsequent discussions without their having to be described multiple times.

4.1 Foreshock Determination

The return electron population is a common and ubiquitous feature of the foreshock. Although its source may vary from reflection at, to leakage through, the bow shock, its presence or absence essentially determines if a spacecraft in the upstream is in the foreshock or in the solar wind. As knowledge of the spacecraft location with respect to these two regions plays an important role in this study, we have developed an effective and simple proxy using the density of the return electron population to provide this information. The method is continuous, sensitive, and can easily be automated to interface with most analysis tools.

~~While in practice one can use the $\phi - \theta$ plots to essentially perform the same task, it is both tedious and time consuming to do so even for relatively short intervals (e.g., 10 minutes).~~ The algorithm we have developed ~~here~~ is based on the assumption that return electrons only exist in the foreshock and not in the solar wind. Under this assumption, if a blind computation of the return electron density is made utilizing a VDF mask of the type shown in the 2nd column of Figure 1, one then expects to see a bi-modal density pattern. High density implies that the spacecraft is located in the foreshock and is seeing reflected electrons. Low density indicates that the spacecraft is located in the solar wind and not reflected electrons are present. This is exactly what is seen. Figure 2, which shows the return density computed for a 40 min period upstream of the bow shock. The left-hand panel in the figure contains the time variations of the density and the right-hand panel which illustrates the bi-modal nature of the data is a plot of the Probability Density Function (PDF) of the same data. To separate the foreshock from solar wind regions, a breakpoint is estimated such that measurements taken when the return density is above the breakpoint indicate times when the spacecraft is in the foreshock. Lower densities indicate being in the solar wind. We estimate of the breakpoint by visual inspection of the $\phi - \theta$ plots. For the example shown, the break point was set to $0.09\,cm^{-3}$, which was used to set the color in the left-hand plot (red when the spacecraft was in the solar wind). The interpretation of the event is not sensitive to small changes in the value chosen for the breakpoint. The breakpoint needs to be set on an event by event basis because of differences in the average density between events. The breakpoint also needs to be reset anytime the energy integration limits are changed. The determination of the spacecraft location (foreshock or solar wind) has a temporal resolution equivalent to the cadence at which the 3D eVDFs are returned (4s in the example in Figure 2), which allows for easy identification of rapid motion of the foreshock boundary. Two final notes:

if the spacecraft is only in one region for an entire event one needs to use a $\phi - \theta$ plot at least at one point in the event to determine if the spacecraft is in the foreshock or solar wind; and if using the density solely as an indicator of region (as opposed to a quantitative measure of the return density) the numerical integration can be started at any energy step that is above the lowest energy at which a return signature is seen the $\phi - \theta$ plots, preferably higher as that tends to produce better separation between the pseudo return densities in the solar wind and return densities in the foreshock.

4.2 Shock Normal

To analytically derive either the expected pitch-angle spread of the return distribution or the expected energy gain in the reflection process requires an estimate of the shock normal. In this study we use the method described in Shen et al. (2007), which is based on the assumption that the shock normal is anti-parallel to the gradient of the magnetic field within the shock front. Gurgiolo et al. (2005) described the multispacecraft methods for computing vector field gradients (curls, vorticity and divergence). Here we implment that approach using 5 vector per second FGM magnetometer field data from the four spacecraft. The result of the analysis is an estimate of the normal vector (in component form in GSE coordinates) with a 1σ deviation given for each component. As with most of the results described in this paper, the method is only valid when the four Cluster spacecraft are in a good tetrahedral configuration (Robert et al., 1998).

4.3 Energization Through Reflection.

To make direct comparisons between the return and strahl populations, it is necessary to remap the return electrons in energy to account for any energy gained in the reflection process. For example if the energization on reflection is a factor of two then the strahl density above ϵ eV should be compared to the return density above 2ϵ eV. The energization can be estimated using the methods described in Sonnerup (1969); Paschmann et al. (1980)to compute the ratio of reflected and incident energies. To implement this method one only needs the direction of the shock normal, as obtained using the Shen et al. technique. Assuming that the reflected electrons are associated with the strahl, which is either parallel or anti-parallel to the magnetic field, knowing the shock normal allows one to estimate the energization directly using Paschmann et al. Eq (9). We computed the energization for a number of shock normals and upstream magnetic field orientations by varying the shock normal direction and the magnetic field direction within a one sigma band about their measured component values.

4.4 Estimated Pitch-Angle Spread of the Reflected Electrons

Under the assumption that the shock is a solid reflective surface, that all reflections are specular, and that the incident strahl guiding center velocity is parallel or anti-parallel to the average magnetic field (depending on whether it is pointing sunward or anti-sunward), it is possible to estimate the pitch-angle spread (over the 4 sec spin period) expected of the return electron distribution. The

230 width is estimated by varying both the shock normal and average magnetic field components within their 1σ bands (as done when estimating the energization in reflection) coupled with a spread in the incident strahl velocity determined from its maximum pitch-angle spread as obtained using the $\phi - \theta$ plots (viz., black outline in the first column of plot in 1). The estimates of the return pitch-angle spread can at times be a bit high when compared to what is observed in the $\phi - \theta$ plots because we

235 use a strahl pitch-angle limit that is generally on the high side to ensure that the total distribution is included in the limits.

4.5 Crossover Energy

In both the solar wind and the foreshock there is often an energy below which the strahl begins to overlap the core-halo and the two populations cannot easily be separated, which we refer to as

240 the crossover energy. Although rarely needed, it is possible to define a crossover energy for the return and core-halo populations. The crossover energy (or sometimes the energy above it) defines the starting energy used in the plasma moment integrations of the isolated populations. In the $\phi - \theta$ plots the crossover energy is characterized by a shift in the population location in the plot. Above the crossover energy, the population is predominantly field-aligned and the strahl is by far the dominant

245 population, while below the cutoff energy the core-halo is dominant and the population shifts to a more radial profile. This is present in all of the upstream eVDFs except at times when there is sufficient separation between the two populations that no crossover energy exists (both populations are fully separable at all energies). The crossover energy may vary from event to event and even within an event with major changes of the magnetic field orientation. For the most part, however, the

250 crossover energy remains reasonably constant within a given event. At times when the interplanetary magnetic field is basically radial, the crossover energy is not easily identifiable, and can be difficult to identify when the field has only a small non-radial component. In most cases, however, the energy at which the shift in dominance between the two populations occurs is unmistakable. The case seen in Figure 1 is a situation in which the magnetic field has only minor non-radial components, making

255 it difficult to identify the cross-over energy, which ~~is~~we estimate to be ~~probably at~~ close to 56.7 or 48.9 eV where the strahl begins to extend~~show a distention~~ to~~ward~~ lower θ.

4.6 Common Figure Formats

We basically use three figure formats to illustrate the plasma characteristics of each of the selected events. These consist of an event overview, a set of $\phi - \theta$ plots illustrating the characteristics of a

260 typical foreshock eVDF during the event, and a plot showing the densities of the total, return, and strahl populations across the time period. All figures of one type share a common format.

- The overview figure (e.g., Figure 3) consists of two panels. The upper panel is the full electron density and total fluid velocity with density plotted against the left axis and velocity against the right axis. Below this is a spectrogram from the PEACE elevation that is closest to the

265   ecliptic overlaid with a plot of the magnetic field. All data are plotted at 4s resolution. Higher
       resolution magnetic field data are included in plots in the discussion section.

   – The characterization of a typical eVDF from the foreshock for the event is shown in a set of
     three columns of $\phi-\theta$ plots (e.g., Figure 4). These form a set of 18 contiguous (in energy)
     $\phi-\theta$ plots, which together cover the energy range from 15.8 to 669.2 eV. White and red traces
270   in each plot are lines of constant pitch-angle and are included basically to delineate where, if
     present in the plots, the strahl (white) and return electron distributions (red) are expected
     to be observed. These are also the same regions used to isolate the two populations in the
     estimation of their plasma moments (viz., Figure 1). The solid dot and triangle in each plot
     are the projection of the head and tail of the magnetic field, respectively. The plots have no
275   smoothing applied to them and display the data in their native $\phi-\theta$ resolution.

   – The density information figure (e.g., Figure 6) contains 2 columns each consisting of 4 rows of
     plots. From top to bottom these are the full, strahl, and return densities and the return to strahl
     density ratio across the event. The left-hand column of plots shows the time variation of the
     quantities while the right-hand column consists of plots of the Probability Density Function
280   (PDF) of the quantities from just the foreshock periods. The average value of the plotted
     quantities for both regions are shown to the right of each PDF plot (foreshock, black text and
     solar wind, red text). If one or the other of the regions is not sampled in the event the average
     value is set to -1.0. In the lower three panels of plots in the first column the red portion(s) of
     the plot indicate times when the spacecraft are in the solar wind and the black portions times
285   when the spacecraft is in the foreshock. This is determined directly from the return electron
     density as discussed in 4.1.

5   Observations

Although we have looked at multiple events as part of this study, we present the detailed results for
only three. These are typical and illustrate most of the important features pertinent to this analysis.

290 ### 5.1   Event 1: 2005-01-11

Figure 3 is the event 1 overview. All data were obtained from C2. The event begins in the mag-
netosheath and at about 15:55 UT the spacecraft passes through the bow shock and enters the fore-
shock. There is only a short stretch of foreshock (about 45s) before the spacecraft crosses into the
solar wind and remains there for most of the rest of the event with the last 90s spent in the foreshock.
295 This is explicitly shown in Figure 6.

   Figure 4 shows a partial representation of a typical foreshock eVDF observed just after the space-
craft crosses the bow shock. Both the strahl and return electron distributions are field-aligned and

9

counter-streaming, the strahl is moving anti-sunward and the return electrons are moving sunward. The white and red traces in each plot are lines of constant pitch-angle of $120°$ ($\equiv 60°$) and $75°$, respectively. The region delimited by the white trace marks the strahl and the region delimited by the red trace marks the return population. Neither population need be present at any given energy.

In this event the crossover energy is located at about 56.7 eV. Above this energy the electron distribution consists almost exclusively of strahl and return particles. Below this energy there is an obvious contribution of core/halo electrons that rapidly becomes the dominant population. There is still a return electron signature below the crossover energy extending probably to as low as 37.7 eV. The return electrons are noticeably non-gyrotropic at the lower energies particularly below the crossover energy where they appear as a partial ring, probably the result of a combination of phase bunching in the reflection process and subsequent gyro-phase mixing and possibly phase locking. As we demonstrate below, it appears that above the crossover energy all of the return electrons originate from the strahl. At lower energies the return electron signature is more likely due to reflection of some percentage of the higher energy halo electrons together with some lower energy strahl that are not fully separable from the core-halo. In the $\phi - \theta$ plots the core/halo population (when present) is centered near $(0°, 0°)$ because it flows radially outward from the sun. (Recall that the spacecraft spin axis is not quite perpendicular to the ecliptic plane.) Halo and strahl electrons that overlap in velocity space will react identically to any external influences.

The angular spread observed in the return electrons in the $\phi - \theta$ plots appears to be consistent with specular or nearly specular reflection. Computation of the shock normal returns a vector of $(0.780 \pm 0.033, 0.603 \pm 0.043, 0.121 \pm 0.098)$ in GSE coordinates, which when coupled with the average magnetic field just upstream of the shock in the foreshock gives a θ_{Bn} of $81°$. Assuming a maximum spread in the strahl pitch-angle of $60°$ we estimate there should be an $81 \pm 5°$ spread in the return electron pitch-angle distribution. The best fit to the return data as determined from the $\phi - \theta$ plots would appear to be a spread of about $75°$ (red trace in Figure 4).

Above the crossover energy the return distribution almost exactly matches the energy range covered by the strahl electrons extending one or two energy steps higher, to energies where there is no evidence of a strahl. At these energies the weak count-rate has the appearance of noise and were it not for the fact that it is observed exclusively within the region in phase space associated with the return distribution it would probably be labeled as such. The higher energy is in all likelihood the manifestation of acceleration in the reflection. That acceleration would put the source of the return electrons below the crossover energy directly within the upper halo.

Using an ensemble of energizations obtained from Eq(9) in Paschmann et al. (1980) we place the average energization factor in the reflection process at 1.17. Figure 5 shows the results as a PDF plot. This value can be used to remap the return electron densities for comparison with the strahl. Under the assumption that above the crossover energy the observed reflected population has the strahl as its source, we compared the estimated strahl density with energies $\geq$70.5 eV with that of the return

335 densities with energies ≥87.5 eV (87.5 eV being the closest center energy being returned to 70.5 x 1.17 = 82.5 eV). We did this by computing the strahl and return densities within each returned energy band and then summing the densities over the energies ≥ 70.5 eV for the strahl and ≥ 87.5 for the return electrons. This mapping is equivalent to an energization factor of 1.24. The results are shown in Figure 6 beginning from just after the shock crossing to 16:30 UT. For this energization

340 mapping, the ratio of return to strahl electrons is 1.04. This was unexpected as the implication is that at least above 70.5 eV there is statistically a full reflection of the strahl at the shock. As a check we increased the starting energies of the density summation up one energy bin for both the strahl and return populations (to 87.5 eV for the strahl and to 110.1 eV for the return electrons which corresponds to an the energization of 1.26), which gives an average density ratio of 1.01.

345 ## 5.2 Event 2: 2005-02-06

Figure 7 shows the overview of event 2. As in the previous event, the spacecraft begins in the magnetosheath and a little before 15:45UT passes through the bow shock and into the foreshock where it stays for a little longer than 2 minutes before entering the solar wind. There are multiple excursions into and out of the foreshock at this point over the rest of the event. Overall the spacecraft

350 spends a significantly larger percentage of time in the foreshock than it did in the previous event, which improves the statistics in the observed return-to-strahl density ratio, as is readily apparent in Figure 9.

The spacecraft were in a good tetrahedral configuration during this event and the shock normal was estimated to be $(0.692 \pm 0.025, 0.161 \pm 0.007, 0.703 \pm 0.027)$ in GSE coordinates. The average

355 magnetic field just upstream of the shock gave a θ_{Bn} of 70°. Using a 50° pitch-angle spread for the strahl we obtained an estimate of the pitch-angle spread for the return electrons of $74 \pm 5°$. The pitch-angle spread determined directly from the $\phi - \theta$ plots in Figure 8 was 75° (the red trace). The white trace used to delineate the strahl is a pitch-angle of 50°.

Comparing Figure 4 with Figure 8 shows only minor differences in the eVDF morphology be-

360 tween the two events. The crossover energy is however, slightly lower in this event, probably 47.9 eV. The return electron signature again extends below the crossover energy down to at least 37.7 eV and is distinctly non-gyrotropic at the lower energy end.

As shown in Figure 9 the energization factor associated with this shock is estimated to be 1.43. Figure 10 shows the electron density profiles of the different populations across Figure 7 starting just

365 after the spacecraft exits the bow shock. In the plot, the strahl density was determined beginning from 56.7 eV and the return density beginning from 87.5 eV. This mapping accounts for an energization factor of about 1.54, which is slightly larger than the analytical estimate. The ratio (1.01) implies that there is full reflection of the strahl in this event at least for this mapping. We looked at two further energy ranges with the strahl density summation beginning at energies 70.5 and 110.1 eV

370 and return density beginning at 87.7 and 139.1 eV (both essentially having mappings equivalent to

11

an energization factor of about 1.57). These give return-to-strahl density ratios of 1.08 and 1.05, respectively.

5.3 Event 3: 2008-04-15

The overview of the third event is shown in Figure 11. Again, the event begins in the magnetosheath with a bow shock crossing at about 19:15 UT. The spacecraft then enters the region upstream of the foreshock (v., Figure 13) and remains there for the rest of the event, with the exception of a short excursion into and out of the solar wind near 19:28 UT. Unfortunately, for this event the 4 spacecraft were not in a good tetrahedral configuration and no estimate of the shock normal was possible. But an estimate of the shock normal is not critical for this event as we have demonstrated in the first two events that the analytically derived values of both the angular width of the return distribution and the reflection energization factor closely match what can be obtained directly from the data.

For this event we obtained a pitch-angle spread of $70°$ for the return electrons directly from the $\phi - \theta$ plots (v., Figure 12) and estimated the reflection energization factor from plots of the density ratio constructed with varying starting integration energies of both the strahl and return populations to be on the order of 1.58 eV. Figure 13 shows the population densities and density ratio constructed with the strahl and return densities beginning at 110.1 eV and 173.1 eV, respectively. This is equivalent to a 1.57 energization factor and gives a density ratio of 0.99. Lowering the beginning energy step in the estimation of both densities to 87.5 and 139.1 eV, respectively (equivalent to a reflection energization factor of 1.59) changes the average ratio to about 1.01. Lowering the starting energy of the two populations one energy step further (equivalent to a reflection energization factor of 1.56) increases the density ratio to about 1.1.

5.4 Errors

There are several recognized sources of error that can affect portions of the event analysis, in particular, the comparisons of the strahl and return densities. Primary among these possible errors is the analytical estimate of the reflection energization factor. The error is purely statistical, resulting from the use of all possible combinations of magnetic field and normal orientations within the 1σ band about the actual component measurements. This value determines the remapping in energy of the return population. As can be seen from Figures 5 and 9, the error is not large, but even small errors can significantly affect the estimation of the measured return-to-strahl density ratio, which depends on the ability to remap the return density in energy. The remapping often splits the starting energy between two energy bins. Depending on which starting point energy is selected in summing up the density moment, one will either over or underestimate the return density, and that factors into the average return-to-strahl density ratio. Another statistical error arises when the spacecraft spends insufficient time in the foreshock to amass a good statistical number for the average return densities. Such errors rise to an overall larger standard deviation in the density ratio. A final source of error

12

that can affect the density ratio arises when only a single estimate of the energization factor per event is obtained at the shock crossing. Changes in the orientation of both the shock normal and upstream magnetic field over the course of an event in reality will continuously change the energization. The remapping used to mesh the return and strahl density estimates is unlikely to remain constant across the event as we currently assume.

6 Discussion

Unlike the solar wind, the foreshock is a region characterized by large amplitude waves and turbulence, which arises, in part, from back-streaming ions and electrons created from the reflection of the incident solar wind off the shock. Both populations are field-aligned and together they provide the necessary free energy to drive a number of instabilities which, e.g., can generate MHD and ULF waves along with Langmuir waves. The instabilities are responsible for the initial scattering and preheating of the solar wind as it approaches the shock.

Ion reflection off the shock is better understood than that of electrons, primarily because it has been studied in greater detail. Simulations have played a substantial role by providing a large number of possible reflection mechanisms, but the simulations have not provided information as to which mechanism(s) are dominant or most important. The results of this study indicate that the reflected electrons are primarily the strahl electrons, which may place limits on some of the available reflection mechanisms. Like the ions, the electrons gain energy in the reflection, as can be seen at the upper energy $\phi - \theta$ plots in Figures 4, 8, and 12. Although the counts are weak in these plots, it is obvious that the return electrons extend a few energy bands higher than the strahl due to energy gained in the reflection process.

The increase in angular width of the return electrons over the incident strahl is consistent with a specular reflection. The same is true of the formation of the partial ring distributions often observed in the lower energy $\phi - \theta$ plots (cf., the top three plots in the first column of Figure 8). This is probably the result of gyro-phase bunching in the reflection process and, if observed far enough upstream, would imply the presence of an active phase trapping mechanism (Gurgiolo et al., 2000, 2005). Electrons phase-mix extremely rapidly, and, coupled with their higher speed, should isotropize significantly closer to the bow shock than do the ions.

While the ratio of the incident and reflected population densities is highly suggestive of a full reflection of the strahl, at least above the crossover energy, there are other indications that lead to the same conclusion and provide even more information about the process. Two of the more obvious questions that can be addressed include where does the reflection occur and how thick is the reflecting region? Answering both questions can be approached by using a series of $\phi - \theta$ plots to monitor the strahl as it approaches the bow shock and observe the changes that occur in the eVDFs.

From an idealistic observational point of view if there is a full reflection of the strahl one might

expect that at some point both it and the return electron population would just drop out of the $\phi - \theta$ plots. Where this occurs would then be the reflection point. If the reflection were sufficiently rapid, occurring within one or two gyroradii, given the spacecraft velocity and the cadence of 3D eVDFs being returned, the reflection would appear from the PEACE data to be almost instantaneous. On the other hand the strahl might be observed to gradually weaken until it is no longer a significant population. The time over which that occurred would represent the thickness of the reflection region.

There are drawbacks to this approach. If there isn't a full reflection of the strahl, then some fraction of it will penetrate into the downstream region, but the return population should still vanish in the $\phi - \theta$ plots after the reflection point. The problem is that it is not obvious that it does. No matter whether the strahl is fully or partially reflected, there will always be a plasma presence downstream of the reflection point and this plasma will, regardless of its source, either be field-aligned or moving radially with the solar wind. Any other flows require the identification of additional forces such as might be provided by the cross shock potential. The problem becomes how to determine if populations seen downstream of the reflection point are the same as or different from the populations seen upstream of the reflection point, in particular, the return electrons.

As there is no guidance on how to differentiate field-aligned electrons downstream of the reflection point from the return electrons upstream of the reflection point we developed a basic set of criteria to use to accomplish this. The criteria stipulate that once it is obvious that reflection point has been crossed an observed population might be a signature of the reflected strahl if:

1. The population in question is field aligned and moving back into the upstream.

2. The population covers approximately the same energy range as the return electrons upstream of the reflection point.

3. The population has roughly the same angular spread as it the return electrons upstream of the reflection point.

4. The population is approximately continuous in time, i.e., not intermittent.

The result of this type of analysis is shown in Figure 14, which contains a column of three spectrograms from PEACE elevation zone 5 (near ecliptic view), one plot corresponding to each of the three analyzed events. Each spectrogram is overlaid by the local magnetic field. These convey similar information to that shown in Figures 3, 7, and 11 but only cover about 2 to 3 minutes of time about the shock crossings to provide for a higher resolution view. The PEACE spectra have been spin averaged and the magnetic field has a 0.2s temporal resolution. In each plot the foot of the shock and shock ramp is clear.

Each crossing has associated with it a pair of arrows labeled **1** and **2**. The position of arrow 2 marks what can be thought of as the most forward boundary of the foreshock as it nears the shock. It is the time of the last unequivocal observation of an electron eVDF that contains both return and

14

strahl populations. At times earlier than arrow 2, there is no observable strahl signature in the $\phi - \theta$ plots, the implication being that arrow 2 marks the location of the reflection point. The absence of the strahl before the reflection point ~~is indicative~~suggests that the strahl is could be fully reflected. There is, however, a return electron signature at and after the time of arrow 1. The return population

480 is either absent or ~~questionable~~unobservable at earlier times ~~earlier than this~~. It should be emphasized that the locations of these arrows are somewhat subjective (arrow 1 much more so than arrow 2).

We are reasonably certain of the placement of arrow 2 in all of the plots (it is obvious when the strahl drops out of the $\phi - \theta$ plots), the location of arrow 1 is more problematic. This arises from the identification of electrons observed prior to arrow 2. We use the 2005-02-06 event to illustrate the

485 problem. Figure 15 contains 7 time sequential columns of $\phi - \theta$ plots each characterizing an eVDF at seven energy steps between 30.1 and 342.7 eV. The energy steps are not sequential but chosen to give the best overall view of where changes on the eVDF are occurring. The figure covers the time frame between 15:43:40.6 to 15:44:05 UT, which includes both arrows in the middle plot in Figure 14. The time of arrow 2 is covered in the seventh column and the time of arrow 1 is covered in the

490 fifth column. The first sweep in each plot is against the left-hand axis which marks the starting time.

Column 7 in the figure is unquestionably from the foreshock as it exhibits both a return and strahl signature down to at least 70.5 eV. The crossover energy is at 56.7 eV and below this there is just a core-halo and a return population signature. The return electrons are anisotropic at the lower energies and that may extend to energies above where it is seen farther upstream (e.g., Figure

495 8). This perhaps is to be expected so close to the reflection point but other than this there is little difference between what is observed in column 7 from what is seen in the eVDFs that follow it in time (not shown). The eVDF in column 6 is very similar to that in column 7 but with a weaker and less defined strahl signature and could probably represent the last foreshock eVDF as well as that of column 7 indicating that the reflection occurs in a very narrow transition region.

500 The first 5 columns show no evidence of a strahl population. There is, however, an electron presence within the strahl mask region, but this is more of a general background than a distinct population. The eVDFs do, however, show sunward propagating field-aligned beam(s) that may or may not consist of reflected electrons. (Although, if they are reflected electrons, it is unclear what the incident particle population is.) One possibility would be that they are upper energy halo electrons.

505 Column 5 appears to be the first column of plots that shows a return electron distribution that is consistent with what is seen after it although it is a bit weaker and less defined at the lower energies. The first 4 eVDFs contain back-streaming electron populations but with prominent and consistent deviations from what is seen in the last three columns of plots. There is, for example, no significant core-halo presence and at times (notably in the second column), no back-streaming electrons at the

510 lower energies. The same features can be seen in earlier eVDFs (not shown here), but they are highly intermittent and exhibit considerable variation in energy and intensity, the latter peaking as would be expected with the increase in density at the shock. Observationally, we do not claim the presence of

15

a return electron signature in the eVDFs as seen in the foreshock earlier than column 5. While this is subjective, it is probably not off by more than 4s. Consequently, while Figure 15 shows that arrow 2 in Figure 14 is reasonably well placed, the placement of arrow 1 at 15:43:57 UT is less certain.

Even with the uncertainty in the placement of arrow 1 in the center plot of Figure 14, it is clear that contrary to the general descriptive phrase "reflection off the shock", the reflection is actually occurring within the foot of the shock and not at, in, or behind the shock front itself. The same is true of the remaining two shock crossings in the figure, although the reflection in event 1 is very close to the ramp. These observations effectively rule out magnetic mirroring as a source of the reflection. First, because there is insufficient ΔB in the foot of the shock to account for any significant mirroring, and second, because there is no observed transition of any portion of the strahl into the region downstream of the reflection point. The strahl are reasonably field-aligned, albeit with a $40°$ to $60°$ spread in pitch-angle, which would preclude the mirroring of a significant percentage of the population. In each of the analyzed events, mirroring would not start until about a pitch-angle of $40° - 50°$ (loss cone), which should leave the bulk of the strahl to penetrate downstream, which is not seen seen in the data. What, exactly, is causing the reflection at the foot of the shock is unclear. At least above the crossover energy, the reflection mechanism is very efficient.

7 Conclusions

Studies of the reflection of the ion solar wind have played a major role in our understanding not only of ~~not only~~ the role of reflections in the physics associated with the foreshock, but also the physics of how the reflection~~it~~ occurs. However, some aspects of ~~the reflection~~that process as gleaned from analyses of ion data may not~~-~~ apply to electrons. A major difference between the upstream features of electrons and ions comes from the strahl. Unlike the ions and the electron core-halo, both of which flow radially outward from the sun, the strahl is field-aligned. Except for times when the interplanetary field is highly radial, the reflection of the strahl need not mimic that of either the ions or of the core-halo. In this study we have found that the reflection of the electron solar wind appears to primarily consist of a reflection of the strahl and that above ~~the~~a crossover energy, ~~the~~ electrons appear to have be~~en~~ fully reflected in the foot of the shock as opposed to in ~~rather than at~~ the shock ramp where the magnetic mirror force would be expected to dominate. In the first event (top panel in Figure 14) there is a small increase in |B| near the breakpoint, but that is not the case in either of the other two events (middle and bottom panels in Figure 14). Consequently, the details of precisely how the reflection occurs are not clear from this analysis, but it must involve primarily the field-aligned component of the distribution, viz., the strahl. One~~It may~~ be have ~~that one will have~~ to study similar events with the higher resolution than is available from Cluster. Data ~~afforded by data~~ from the Magnetospheric Multiscale mission (MMS) may be useful in further elucidating the details of how the strahl is reflected in these quasi-paerpendicular shock geometries. Based on the

agreement between the observed spread in the return pitch-angle with analytically produced spreads, we ~~find~~conclude that the reflection is specular. Below the breakpoint energy we cannot rule out a partial reflection of the upper energy halo electrons or of strahl electrons, which may be mixed in with them. These two populations cannot be separated in our analysis at energies below the crossover energy.

The analysis and identification of just where the spacecraft were during the event was facilitated, in part, by ~~As part of~~ the development of ~~our analysis, we were led to~~ an ~~One of the results of this study has been the~~ algorithm that helped greatly ~~developed to help~~ in determin~~ing~~e when the data came from times when the spacecraft were ~~are~~ in the foreshock as opposed to the solar wind. The basic assumption ~~at algorithm~~ is ~~based on the assumption~~ that return electrons only exist in the foreshock. Consequently, when one sees a bi-modal density pattern, the spacecraft is, perforce, in the foreshock. When the density is low and the pattern is not bi-modal the spacecraft is in the solar wind and, conversely, when density is high (and not bi-modal)~~ low and not bi-modal, then~~ the spacecraft is in the solar wind. The pattern is shown in Figure fig:FsSWmask. ~~Consequently~~Thus, an effective approach ~~,~~to separat~~ing~~e the foreshock periods from solar wind periods, ~~one~~is to set~~s~~ a breakpoint such that one is in the foreshock when the density is higher than th~~at~~e breakpoint, but ~~one is~~ in the solar wind when the density is ~~lower~~below tha~~n~~ the breakpoint. The precise value of that breakpoint is not critical as the examples we found indicate that the density values in the two modes are generally quite distinct.

Future studies using high resolution data obtained in the foreshock should add to the number of events and help to determine precisely how solar wind electrons are reflected at Earth's bow shock.

References

Anderson, K. A., Lin, R. P., Gurgiolo, C., Parks, G. K., Potter, D. W., Werden, S., and Rème, H.: A component of nongyrotropic (phase bunched) electrons upstream from the Earth's bow shock, JGR, 90, 10 809, 1985.

Bale, S. D., Burgess, D., Kellogg, P. J., Goetz, K., and Monson, S. J.: On the amplitude of intense Langmuir waves in the terrestrial electron foreshock, JGR, 102, 11 281–11 286, doi:10.1029/97JA00938, 1997.

Balogh, A., Dunlop, M. W., Cowley, S. W. H., Southwood, D. J., Thomlinson, J. G., Glassmeier, K. H., Musmann, G., Luhr, H., Buchert, S., Acuna, M. H., Fairfield, D. H., Slavin, J. A., Riedler, W., Schwingenschuh, K., and Kivelson, M. G.: The Cluster Magnetic Field Investigation, Space Science Reviews, 79, 65–91, doi:10.1023/A:1004970907748, 1997.

Bonifazi, C. and Moreno, G.: Reflected and diffuse ions backstreaming from the earth's bow shock, 1, Basic Properties, JGR, 86, 4397, 1981a.

Bonifazi, C. and Moreno, G.: Reflected and diffuse ions backstreaming from the earth's bow shock, 2, Origin, JGR, 86, 4405, 1981b.

Burgess, D.: Simulations of backstreaming ion beams formed at oblique shocks by direct reflection, Ann. Geophys., 5, 133–145, 1987.

Burgess, D. and Schwartz, S. J.: The dynamics and upstream distributions of ions reflected at the Earth's bow shock, JGR, 89, 7407, 1984.

Décréau, P. M. E., Fergeau, P., Krannosels'kikh, V., Leveque, M., Martin, P., Randriamboarison, O., Sene, F. X., Trotignon, J. G., Canu, P., and Mogensen, P. B.: Whisper, a Resonance Sounder and Wave Analyser: Performances and Perspectives for the Cluster Mission, Space Science Reviews, v. 79, Issue 1/2, p. 157-193., 79, 157–193, doi:10.1023/A:1004931326404, 1997.

Fazakerley, A. N., Lahiff, A. D., Wilson, R. J., Rozum, I., Anekallu, C., West, M., and Bacai, H.: PEACE Data in the Cluster Active Archive, The Cluster Active Archive, Studying the Earth's Space Plasma Environment. Edited by H. Laakso, M.G.T.T. Taylor, and C. P. Escoubet. Astrophysics and Space Science Proceedings, Berlin: Springer, 11, 129–144, doi:10.1007/978-90-481-3499-1_8, 2010.

Fitzenreiter, R. J., Viñas, A. F., Klimas, A. J., Lepping, R. P., Kaiser, M. L., and Onsager, T. G.: Wind observations of the electron foreshock, Geophysical Research Letters, Volume 23, Issue 10, p. 1235-1238, 23, 1235–1238, doi:10.1029/96GL00826, 1996.

Fuselier, S. A. and Schmidt, W. K. H.: H+ and He2+ heating at the Earth's bow shock, Journal of Geophysical Research, Volume 99, Issue A6, p. 11539-11546, 99, 11 539–11 546, doi:10.1029/94JA00350, 1994.

Gedalin, M.: Transmitted, reflected, quasi-reflected, and multiply reflected ions in low-Mach number shocks, Journal of Geophysical Research: Space Physics, 121, 10 754–10 767, doi:10.1002/2016JA023395, 2016.

Gloag, J. M., Lucek, E. A., Alconcel, L.-N., Balogh, A., Brown, P., Carr, C. M., Dunford, C. N., Oddy, T., and Soucek, J.: FGM Data Products in the CAA, The Cluster Active Archive, Studying the Earth's Space Plasma Environment. Edited by H. Laakso, M.G.T.T. Taylor, and C. P. Escoubet. Astrophysics and Space Science Proceedings, Berlin: Springer, 11, 109–128, doi:10.1007/978-90-481-3499-1_7, 2010.

Gosling, J. T., Asbridge, J. R., Bame, S. J., Paschmann, G., and Sckopke, N.: Observations of two distinct populations of bow shock ions in the upstream solar wind, GRL, 5, 957, 1978.

Gosling, J. T., Thomsen, M. F., Bame, S. J., Feldman, W. C., Paschmann, G., and Sckopke, N.: Evidence for specularly reflected ions upstream from the quasi-parallel bow shock, Geophysical Research Letters, vol. 9,

18

615   Dec. 1982, p. 1333-1336. Research supported by the U.S. Department of Energy and Bundesministerium für Forschung und Technologie;, 9, 1333–1336, doi:10.1029/GL009i012p01333, 1982.

Gosling, J. T., Thomsen, M. F., Bame, S. J., and Russell, C. T.: Suprathermal electrons at the Earth's bow shock, JGR, 94, 10 011–10 025, 1989.

Greenstadt, E. W., Le, G., and Strangeway, R. J.: ULF waves in the foreshock, ASR, 15, 71–84, 1995.

620   Gurgiolo, C. and Goldstein, M. L.: Observations of diffusion in the electron halo and strahl, Annales Geophysicae, Volume 34, Issue 12, 2016, pp.1175-1189, 34, 1175–1189, doi:10.5194/angeo-34-1175-2016, 2016.

Gurgiolo, C., Parks, G. K., and Mauk, B. H.: Upstream gyrophase bunched ions: A mechanism for creation at the bow shock and the growth of velocity space structure through gyrophase mixing, JGR, 88, 9093, 1983.

Gurgiolo, C., Wong, H. K., and Winske, D.: Low and high frequency waves generated by gyrophase bunched
625   ions at oblique shocks, Geophysical Research Letters, 20, 783–786, doi:10.1029/93GL00854, 1993.

Gurgiolo, C., Larson, D., Lin, R. P., and Wong, H. K.: A gyrophase-bunched electron signature upstream of the Earth's bow shock, GRL, 27, 3153, 2000.

Gurgiolo, C., Goldstein, M. L., Narita, Y., Glassmeier, K. H., and Fazakerley, A. N.: A phase locking mechanism for non-gyrotropic electron distributions upstream of the Earth's bow shock, JGR, 110, A06206, doi:
630   10.1029/2004JA011010, 2005.

Gurgiolo, C., Goldstein, M. L., Viñas, A. F., and Fazakerley, A. N.: First measurements of electron vorticity in the foreshock and solar wind, AG, 28, 2187–2200, doi:10.5194/angeo-28-2187-2010, 2010.

Gurnett, D. A. and Frank, L. A.: Ion acoustic waves in the solar wind, Journal of Geophysical Research, vol. 83, Jan. 1, 1978, p. 58-74. Navy-supported research;, 83, 58–74, doi:10.1029/JA083iA01p00058, 1978.

635   Gustafsson, G., Bostrom, R., Holback, B., Holmgren, G., Lundgren, A., Stasiewicz, K., Ahlen, L., Mozer, F. S., Pankow, D., Harvey, P., Berg, P., Ulrich, R., Pedersen, A., Schmidt, R., Butler, A., Fransen, A. W. C., Klinge, D., Thomsen, M., Falthammar, C.-G., Lindqvist, P.-A., Christenson, S., Holtet, J., Lybekk, B., Sten, T. A., Tanskanen, P., Lappalainen, K., and Wygant, J.: The Electric Field and Wave Experiment for the Cluster Mission, Space Science Reviews, 79, 137–156, doi:10.1023/A:1004975108657, 1997.

640   Hoppe, M. and Russell, C. T.: Whistler mode wave packets in the earth's foreshock region, Nature, vol. 287, Oct. 2, 1980, p. 417-420., 287, 417–420, doi:10.1038/287417a0, 1980.

Hoppe, M. M., Russell, C. T., Frank, L. A., Eastman, T. E., and Greenstadt, E. W.: Upstream hydromagnetic waves and their association with backstreaming ion populations: ISEE 1 and 2 observations, JGR, 86, 4471–4492, 1981.

645   Johnstone, A. D., Alsop, C., Burge, S., Carter, P. J., Coates, A. J., Coker, A. J., Fazakerley, A. N., Grande, M., Gowen, R. A., Gurgiolo, C., Hancock, B. K., Narheim, B., Preece, A., Sheather, P. H., Winningham, J. D., and Woodliffe, R. D.: Peace: a Plasma Electron and Current Experiment, Space Science Reviews, 79, 351–398, doi:10.1023/A:1004938001388, 1997.

Khotyaintsev, Y., Lindqvist, P.-A., Eriksson, A., and André, M.: The EFW Data in the CAA, The Cluster
650   Active Archive, Studying the Earth's Space Plasma Environment. Edited by H. Laakso, M.G.T.T. Taylor, and C. P. Escoubet. Astrophysics and Space Science Proceedings, Berlin: Springer, 11, 97–108, doi:10. 1007/978-90-481-3499-1_6, 2010.

Kis, A., Scholer, M., Klecker, B., Kucharek, H., Lucek, E. A., and Rème, H.: Scattering of field-aligned beam ions upstream of Earth's bow shock, Annales Geophysicae, Volume 25, Issue 3, 2007, pp.785-799, 25, 785–

655   799, doi:10.5194/angeo-25-785-2007, 2007.

Krauss-Varban, D. and Wu, C. S.: Fast Fermi and gradient drift acceleration of electrons at nearly perpendicular
collisionless shocks, Journal of Geophysical Research (ISSN 0148-0227), vol. 94, Nov. 1, 1989, p. 15367-
15372., 94, 15 367–15 372, doi:10.1029/JA094iA11p15367, 1989.

Kucharek, H., Möbius, E., Scholer, M., Mouikis, C., Kistler, L., Horbury, T., Balogh, A., Réme, H., and
660   Bosqued, J.: On the origin of field-aligned beams at the quasi-perpendicular bow shock: multi-spacecraft
observations by Cluster, Annales Geophysicae, vol. 22, Issue 7, pp.2301-2308, 22, 2301–2308, doi:10.5194/
angeo-22-2301-2004, 2004.

Larson, D. E., Lin, R. P., McFadden, J. P., Ergun, R. E., Carlson, C. W., Anderson, K. A., Phan, T. D., McCarthy,
M. P., Parks, G. K., Rème, H., Bosqued, J. M., d'Uston, C., Sanderson, T. R., Wenzel, K. P., and Lepping,
665   R. P.: Probing the Earth's bow shock with upstream electrons, Geophysical Research Letters, 23, 2203–2206,
doi:10.1029/96GL02382, 1996.

Leroy, M. M. and Mangeney, A.: A theory of energization of solar wind electrons by the earth's bow shock,
Annales Geophysicae, 2, 449–456, 1984.

Leroy, M. M., Goodrich, C. C., Winske, D., Wu, C. S., and Papadopoulos, K.: Simulation of a perpendicular
670   bow shock, Geophysical Research Letters, 8, 1269–1272, doi:10.1029/GL008i012p01269, 1981.

Leroy, M. M., Winske, D., Goodrich, C. C., Wu, C. S., and Papadopoulos, K.: The structure of perpendicular
bow shocks, Journal of Geophysical Research, vol. 87, July 1, 1982, p. 5081-5094., 87, 5081–5094, doi:
10.1029/JA087iA07p05081, 1982.

Mesiane, K., Mazelle, C., Lin, R. P., LeQuéau, D., Larson, D. E., Parks, G. K., and Lepping, R. P.: Three-
675   dimensional observations of gyrating ion distributions far upstream of the Earth's bow shock and their asso-
ciation with low-frequency waves, JGR, 106, 5731–5742, 2001.

Meziane, K., Mazelle, C., Wilber, M., Le Quéau, D., Eastwood, J., Rème, H., Dandouras, I., Sauvaud, J.,
Bosqued, J., Parks, G., Kistler, L., McCarthy, M., Klecker, B., Korth, A., Bavassano-Cattaneo, M., Lundin,
R., and Balogh, A.: Bow shock specularly reflected ions in the presence of low-frequency electromagnetic
680   waves: a case study, Annales Geophysicae, vol. 22, Issue 7, pp.2325-2335, 22, 2325–2335, doi:10.5194/
angeo-22-2325-2004, 2004.

Paschmann, G. and Sckopke, N.: Ion reflection and heating at the Earth's bow shock, in: Topics in plasma-
astro-, and space physics, edited by Haerendel, G. and Battrick, B., p. 139, Max-Plank-Institute fur Physik
and Astrophysik, Garching, Federal Republic of Germany, 1983.

685   Paschmann, G., Sckopke, N., Asbridge, J. R., Bame, S. J., and Gosling, J. T.: Energization of solar wind ions by
reflection from the earth's bow shock, Journal of Geophysical Research, vol. 85, Sept. 1, 1980, p. 4689-4693.
Research sponsored by the U.S. Department of Energy; Bundesministerium für Forschung und Technologie,
85, 4689–4693, doi:10.1029/JA085iA09p04689, 1980.

Paschmann, G., Sckopke, N., Papamastorakis, I., Asbridge, J. R., Bame, S. J., and Gosling, J. T.: Char-
690   acteristics of reflected and diffuse ions upstream from the earth's bow shock, Upstream Wave and Par-
ticle Workshop, California Institute of Technology, Jet Propulsion Laboratory, Pasadena, CA, Apr. 15,
16, 1980. Journal of Geophysical Research, vol. 86, June 1, 1981, p. 4355-4364. Research sponsored by
the U.S. Department of Energy; Bundesministerium für Forschung und Technologie, 86, 4355–4364, doi:
10.1029/JA086iA06p04355, 1981.

695   Robert, P., Roux, A., Harvey, C. C., Dunlop, M. W., Daly, P. W., and Glassmeier, K. H.: Tetrahedron Geometry
Factors, in: Analysis methods for multi-spacecraft data, edited by Paschmann, G. and Daly, P. W., pp. 323–
348, ESA Publications Division, Keplerlaan 1, 2200 AG Noordwijk, The Netherlands, 1998.

Russell, C. T., Childers, D. D., and Coleman, P. J., J.: Ogo 5 observations of upstream waves in the in-
terplanetary medium: Discrete wave packets, Journal of Geophysical Research, 76, 845, doi:10.1029/
700   JA076i004p00845, 1971.

Savoini, P., Lembége, B., and Stienlet, J.: Origin of backstreaming electrons within the quasi-perpendicular
foreshock region: Two-dimensional self-consistent PIC simulation, Journal of Geophysical Research, Vol-
ume 115, Issue A9, CiteID A09104, 115, A09 104, doi:10.1029/2010JA015263, 2010.

Scholer, M. and Terasawa, T.: Ion reflection and dissipation at quasi-parallel collisionless shocks, Geophys.
705   Res. Lett., 17, 119–122, doi:10.1029/GL017i002p00119, 1990.

Schwartz, S. J. and Marsch, E.: The radial evolution of a single solar wind plasma parcel, Journal of Geophys-
ical Research (ISSN 0148-0227), vol. 88, Dec. 1, 1983, p. 9919-9932. Research supported by the Nuffield
Foundation., 88, 9919–9932, doi:10.1029/JA088iA12p09919, 1983.

Shen, C., Dunlop, M., Li, X., Liu, Z. X., Balogh, A., Zhang, T. L., Carr, C. M., Shi, Q. Q., and Chen, Z. Q.:
710   New approach for determining the normal of the bow shock based on Cluster four-point magnetic field
measurements, Journal of Geophysical Research: Space Physics, Volume 112, Issue A3, CiteID A03201,
112, A03 201, doi:10.1029/2006JA011699, 2007.

Smith, C. W., Goldstein, M. L., Gary, S. P., and Russell, C. T.: Beam-driven ion cyclotron harmonic resonances
in the terrestrial foreshock, Journal of Geophysical Research (ISSN 0148-0227), vol. 90, Feb. 1, 1985, p.
715   1429-1434. NASA-supported research., 90, 1429–1434, doi:10.1029/JA090iA02p01429, 1985.

Sonnerup, B.: Acceleration of particles reflected at a shock front, Journal of Geophysical Research, Space
Physics, 74, 1301–1304, doi:10.1029/JA074i005p01301, 1969.

Thomsen, M. F.: Upstream suprathermal ions, in: Collision Shocks in the Heliosphere: Reviews of Current
Research, Geophys. Monograph 35, pp. 253–270, American Geophysical Union, Washington DC, USA,
720   doi:10.1029/GM035p0253, 1985.

Thomsen, M. F., Schwartz, S. J., and Gosling, J. T.: Observational evidence on the origin of ions upstream of the
earth's bow shock, Journal of Geophysical Research (ISSN 0148-0227), vol. 88, Oct. 1, 1983, p. 7843-7852.
Research supported by the U.S. Department of Energy., 88, 7843–7852, doi:10.1029/JA088iA10p07843,
1983.

725   Trotignon, J. G., Décréau, P. M. E., Rauch, J. L., Vallières, X., Rochel, A., Kougblénou, S., Lointier, G., Facskó,
G., Canu, P., Darrouzet, F., and Masson, A.: The WHISPER Relaxation Sounder and the CLUSTER Active
Archive, The Cluster Active Archive, Studying the Earth's Space Plasma Environment. Edited by H. Laakso,
M.G.T.T. Taylor, and C. P. Escoubet. Astrophysics and Space Science Proceedings, Berlin: Springer, 11,
185–208, doi:10.1007/978-90-481-3499-1_12, 2010.

730   Yuan, X., Cairns, I. H., Robinson, P. A., and Kuncic, Z.: Effects of overshoots on electron distributions up-
stream and downstream of quasi-perpendicular collisionless shocks, Journal of Geophysical Research: Space
Physics, Volume 112, Issue A5, CiteID A05108, 112, A05 108, doi:10.1029/2006JA011684, 2007.

Zhang, Y., Matsumoto, H., and Kojima, H.: Bursts of whistler mode waves in the upstream of the bow shock:
Geotail observations, Journal of Geophysical Research, Volume 103, Issue A9, p. 20529-20540, 103, 20 529–

735   20 540, doi:10.1029/98JA01371, 1998.
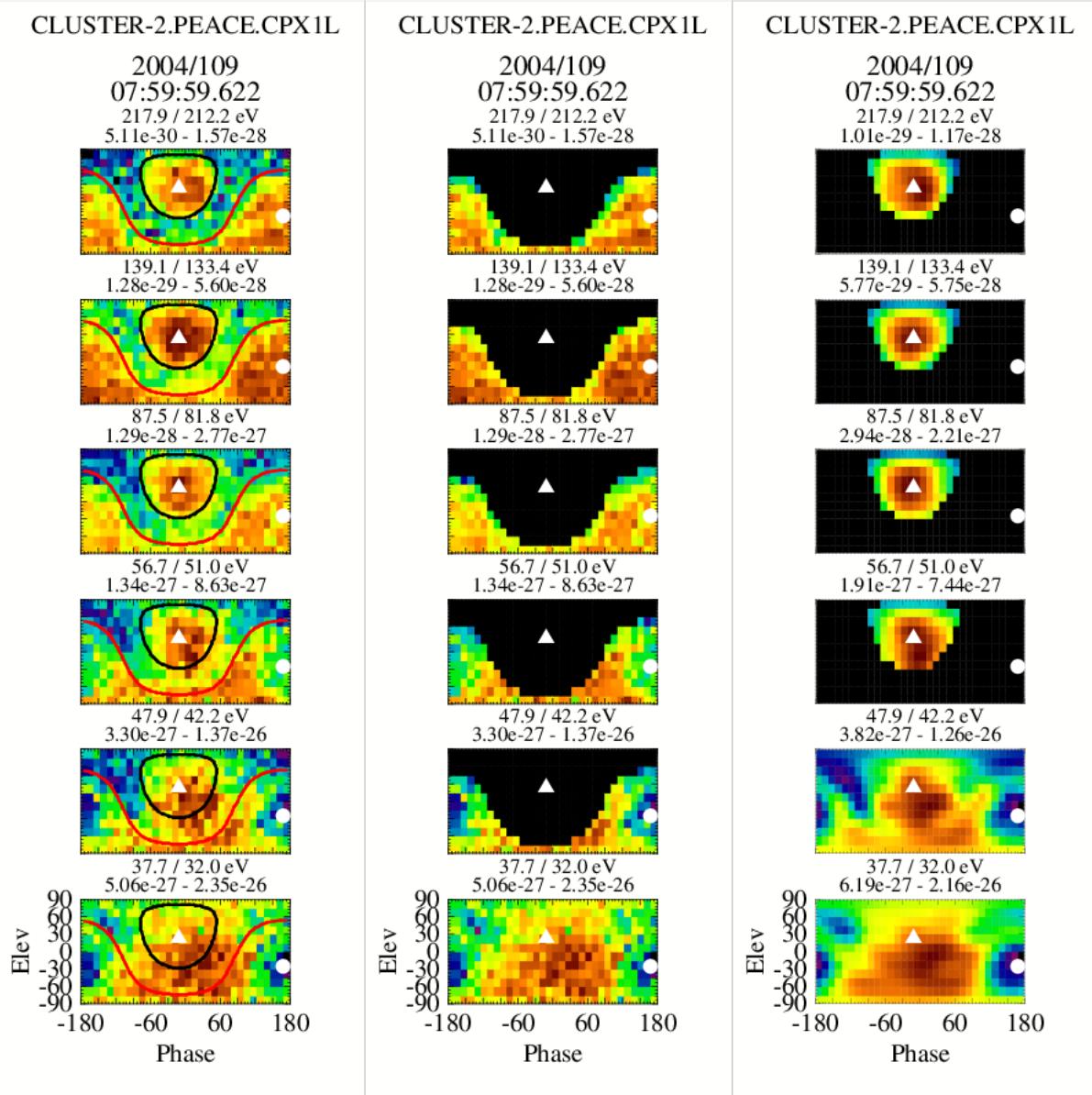
Fig. 1. A set of 3 columns of $\phi - \theta$ plots illustrating the use of phase space masks to isolate various electron populations. The first column shows a set of plots with no masking. The black and red traces are lines of constant pitch-angle of $120°$ and $80°$ respectively. The second column of plot masks out all pitch-angles greater than $80°$ and at energies greater than 37.7 eV leaving just the return electrons. The third column of plot masks out all pitch-angles less than $120°$ and at energies greater than 47.9 eV leaving just the strahl electrons. The solid triangle and dot in the plots are the projections of the tail and head of the magnetic field vector, respectively.
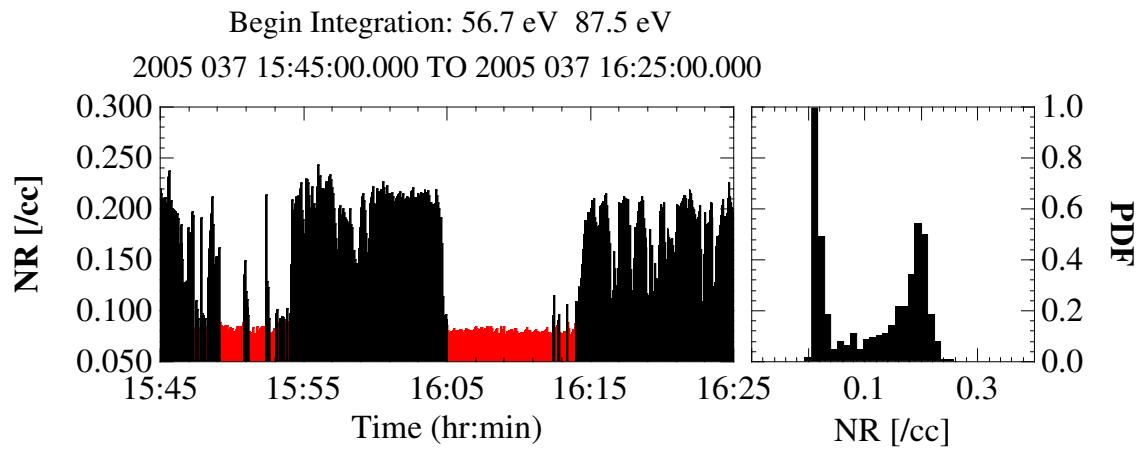
Fig. 2. Figure demonstrates the bi-modal aspect of the return electron density upstream of the bow shock. The right-hand plot is a PDF computed for a 40 minute stretch when Cluster-2 was upstream of the shock. The two bi-modal peaks are obvious. The left-hand plot shows the time dependence of the same data. Red indicates when the spacecraft is in the solar wind, which was determined using a 0.09 cm^{-3} breakpoint in the return density.
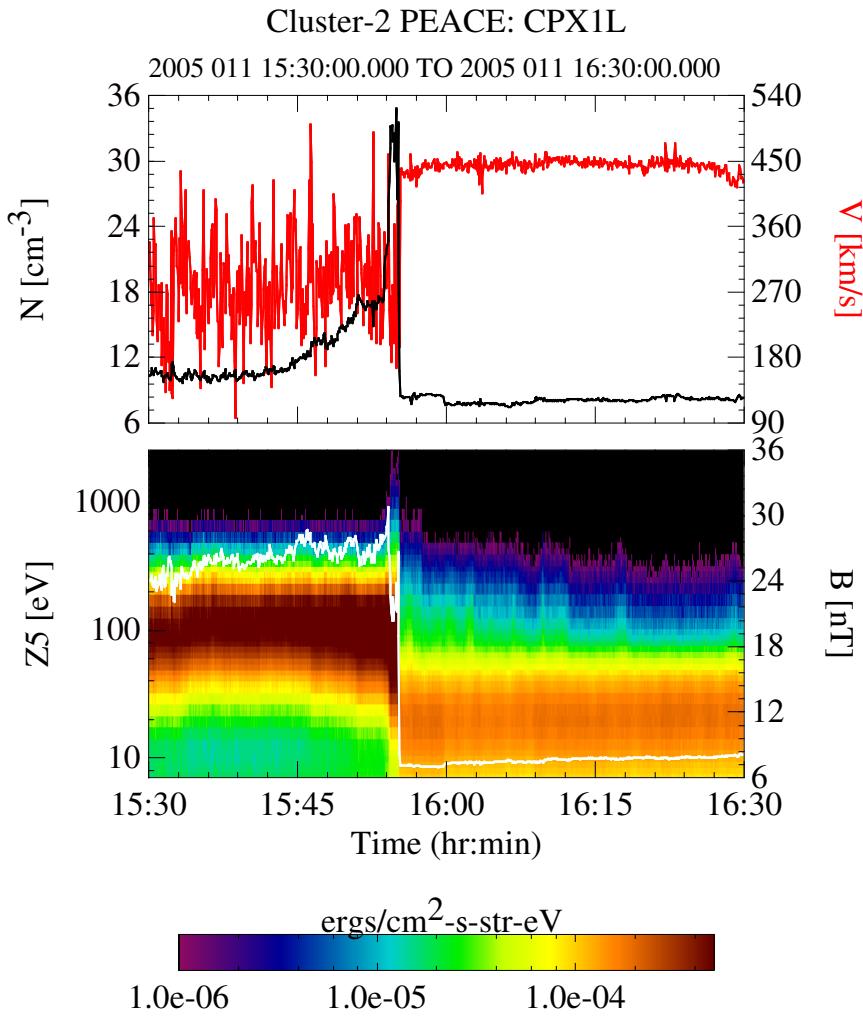
Fig. 3. An overview of the 2005-01-11 event. The lower panel shows an energy spectrogram of the electron data from one of the near ecliptic heads of PEACE overlaid by a trace of the magnetic field (white). The upper panel contains the full electron density (black) and the bulk fluid velocity (red). All data were from C2. At 15:55 the spacecraft exits the magnetosheath, passes through the bow shock and enters the upstream solar wind. For about the first minute the spacecraft is in the foreshock and then transitions into the solar wind, staying there for most of the remaining time period.
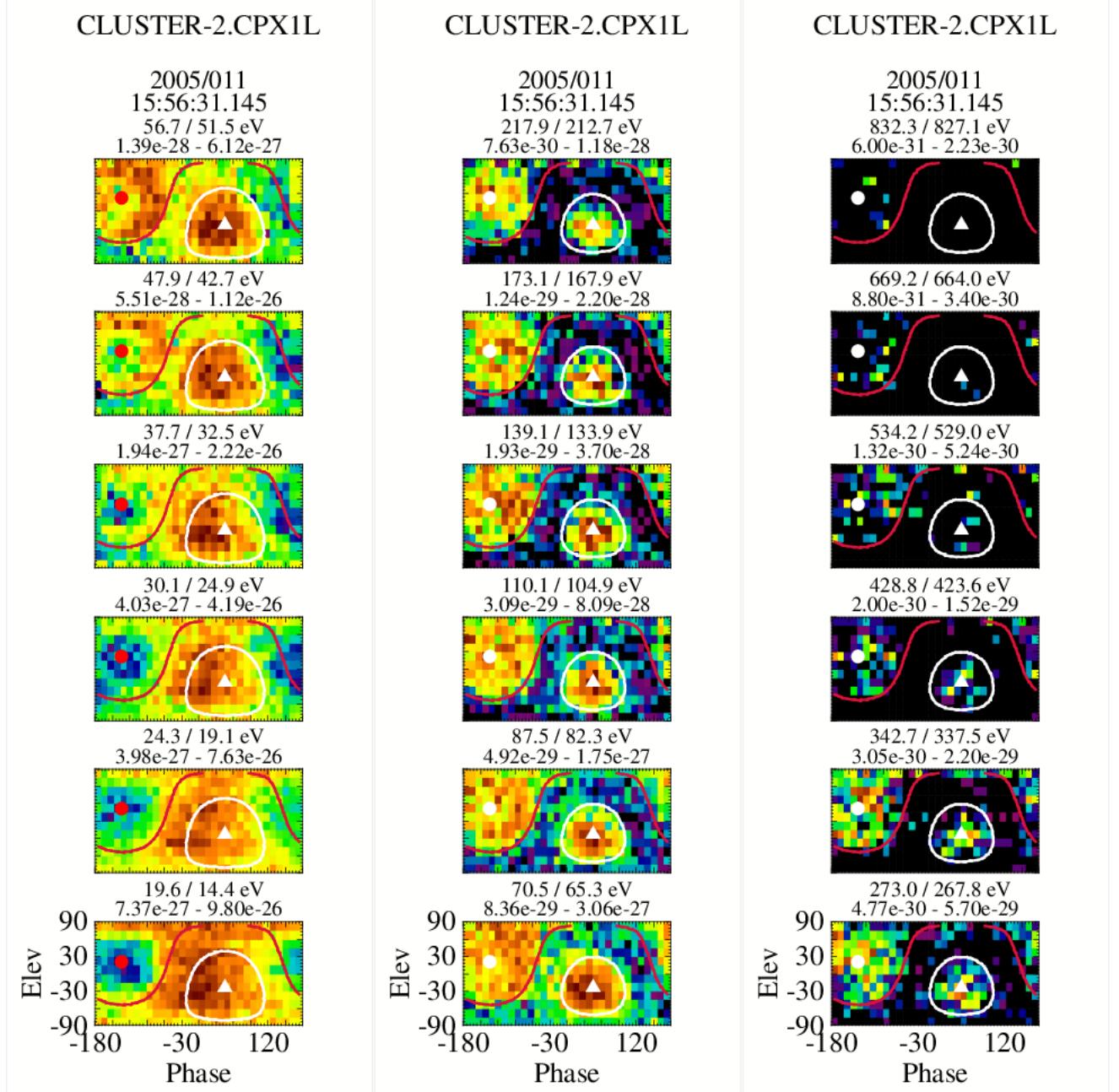
Fig. 4. A set of $\phi - \theta$ plots showing each energy step from 15.8 to 669.2 eV from a single eVDF in the foreshock. The white and red traces are lines of constant pitch-angle (120° and 75°, respectively) and are shown solely to indicate the areas where the strahl (white) and return electrons (red) might be expected to be found. The presence of either population may not exist at any given energy.

2005-01-11

Energy Gain on Reflection
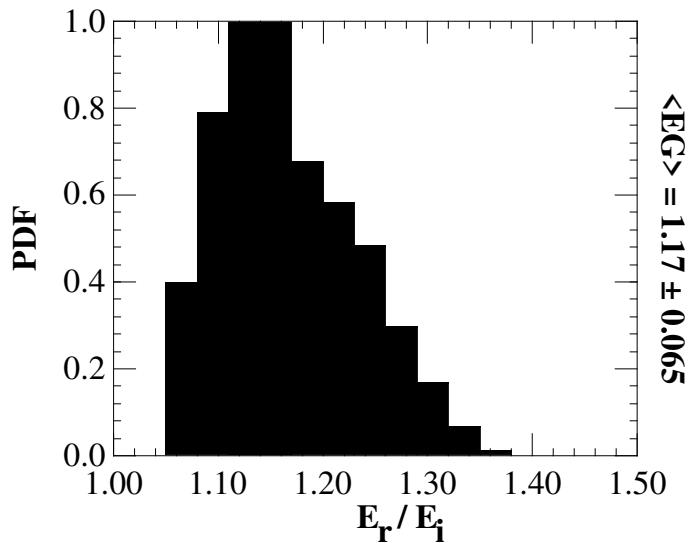
Fig. 5. PDF plot of the energy gain on reflection from the bow shock. The PDF was formed from the results of the energization model by varying the shock normal and magnetic field components within a 1σ band about their average values. The average energization and the 1σ value are shown to the right of the plot.
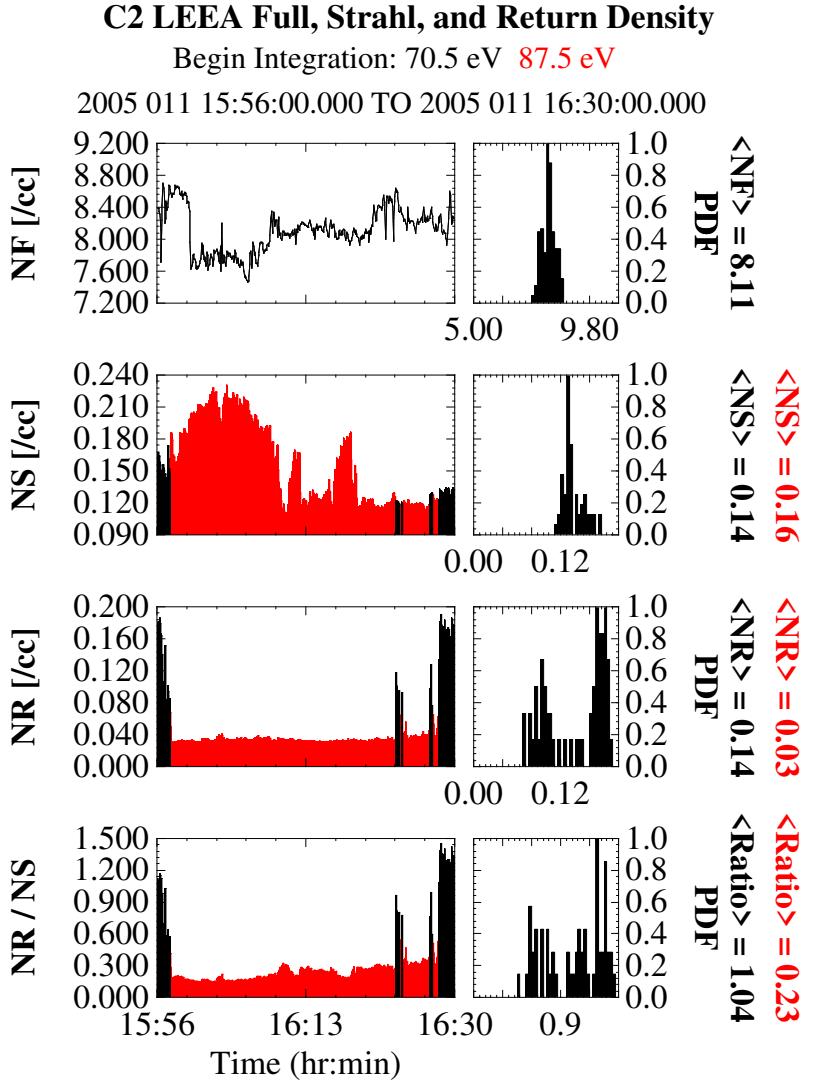
Fig. 6. Electron density information across the 2005-01-11 event. From top to bottom, the total, strahl and return electron densities and the ratio of the return to strahl density across the event. The left-hand column of plots show the values as a function of time. The red portions in the lower three panels show when the spacecraft was in the solar wind. The right-hand column of plots are the corresponding PDF plots of the foreshock density only. The average foreshock and solar wind densities are shown to the right of each PDF plot (red solar wind, black foreshock). The beginning energy integration used to estimate the density in each region is shown at the top.
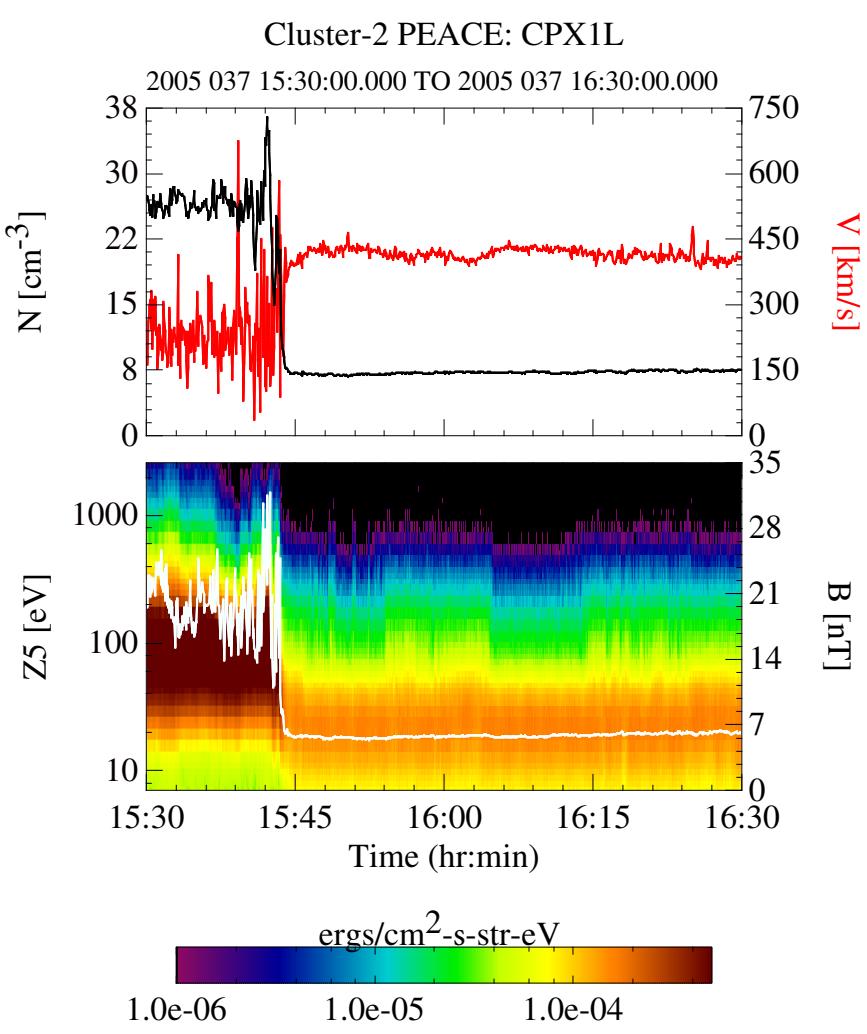
Fig. 7. An overview of the 2005-02-06 event. The lower panel shows an energy spectrogram of the electron data from one of the near ecliptic heads of PEACE overlaid by a trace of the magnetic field (white). The upper panel contains the full electron density (black) and the bulk fluid velocity (red). All data were from C2. At 15:45 the spacecraft exits the magnetosheath, passes through the bow shock and enters the upstream solar wind. For about the two minutes the spacecraft is in the foreshock and then transitions into the solar wind. There are two major periods of solar wind before the end of the event that can be seen in Figure 10.
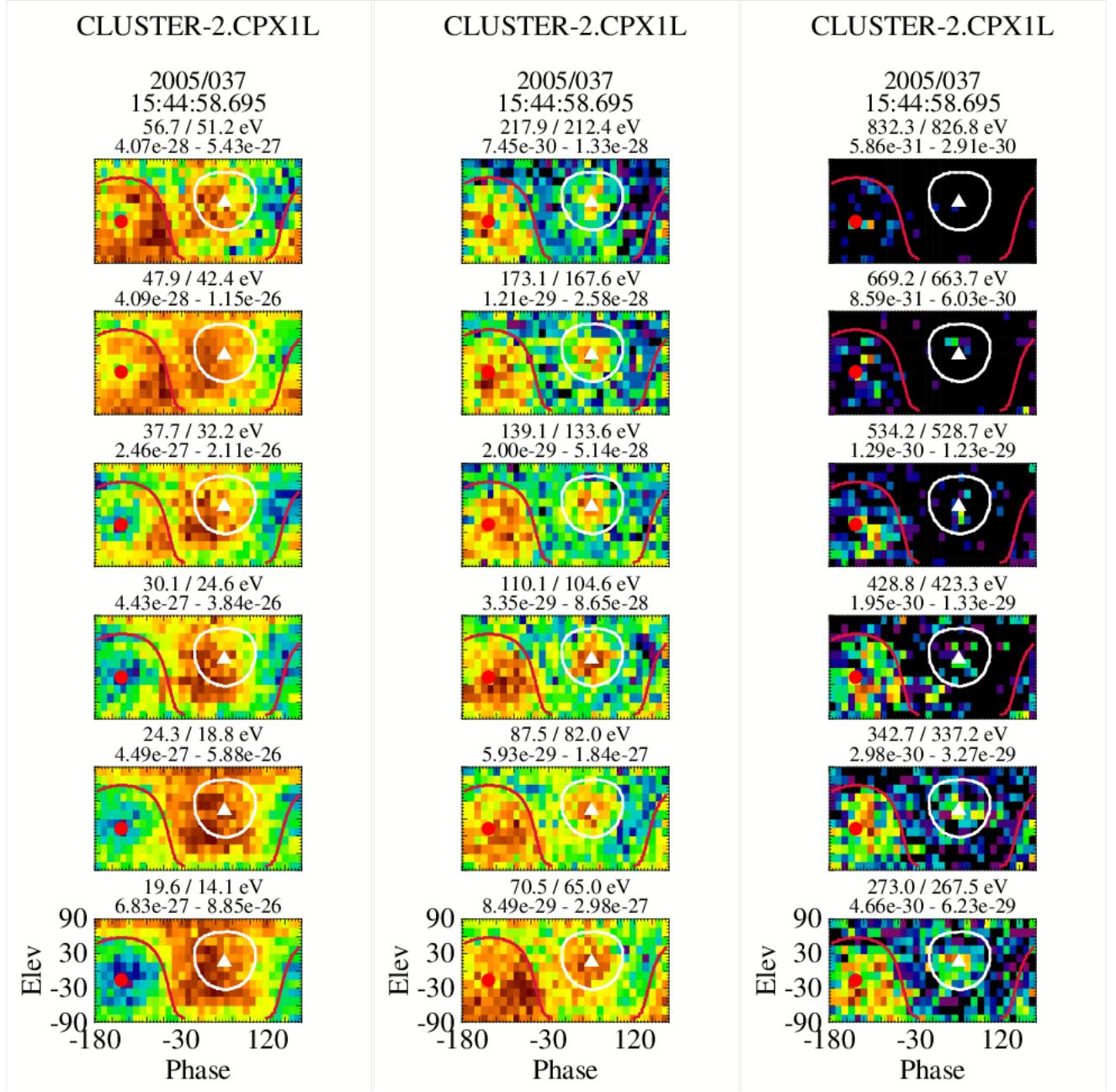
Fig. 8. A set of $\phi - \theta$ plots showing each energy step from 15.8 to 669.2 eV from a single eVDF in the foreshock. The white and red traces are lines of constant pitch-angle (130 and 75 degrees respectively) and are shown solely to indicate the areas where the strahl (red) and return electrons (white) might be expected to be found. The presence of either population may not exist at any given energy. The solid triangle and dot in the plots are the projections of the tail and head of the magnetic field vector respectively.

2005-02-06
Energy Gain on Reflection

Fig. 9. PDF plot of the energy gain on reflection from the bow shock. The PDF was formed from the results of the energization model by varying the shock normal and magnetic field components within a 1σ band about their average values. The average energization and the 1σ value are shown to the right of the plot.

C2 LEEA Full, Strahl, and Return Density

Begin Integration: 56.7 eV 87.5 eV

2005 037 15:45:00.000 TO 2005 037 16:30:00.000
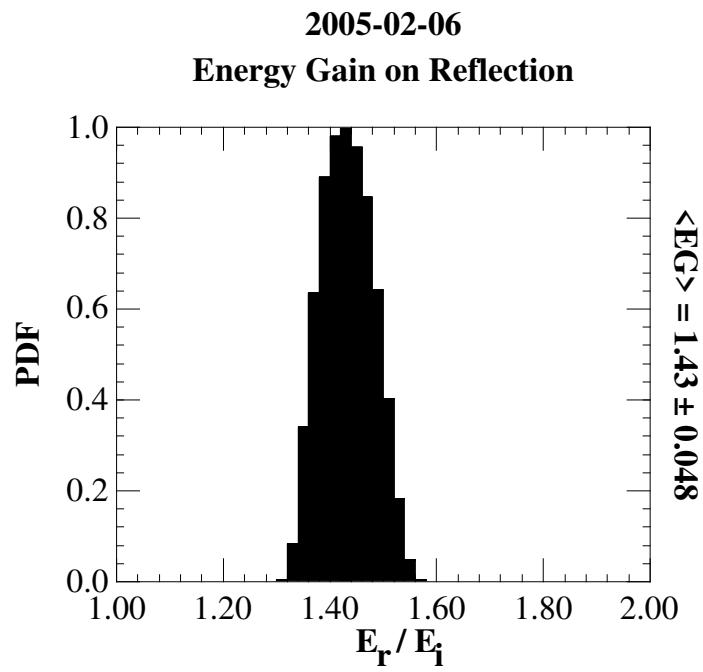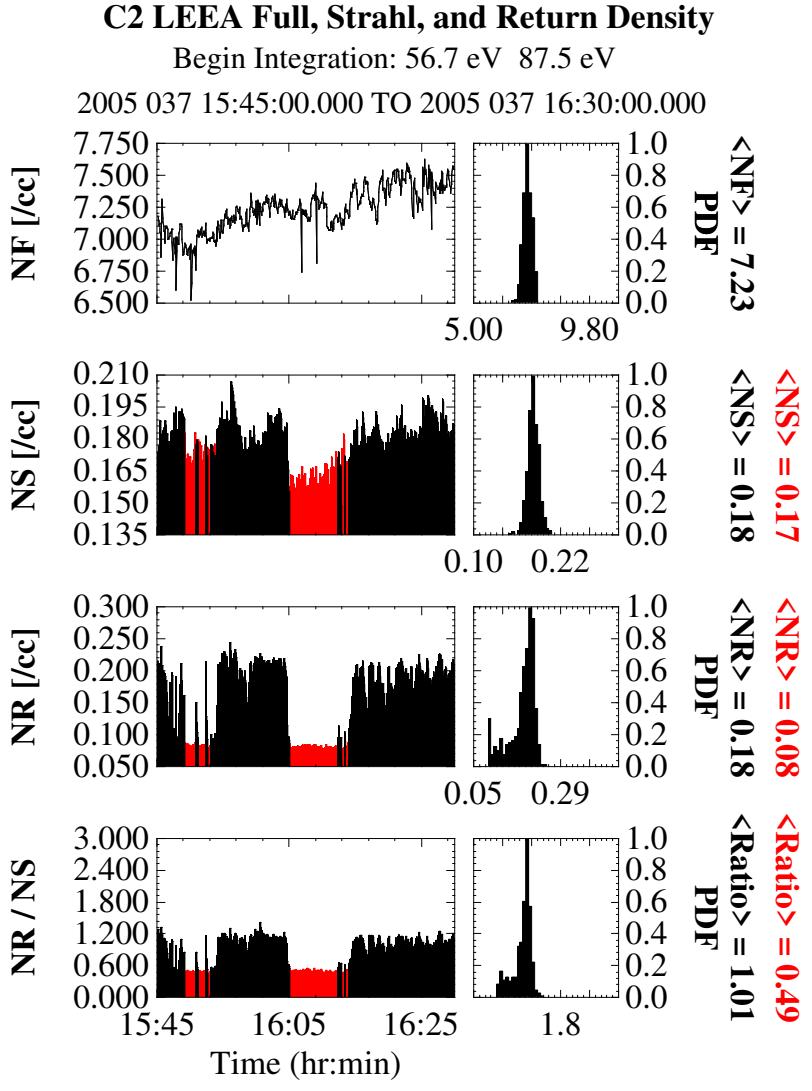
Fig. 10. Electron density information across the 2005-02-06 event. From top to bottom, the total, strahl and return electron densities and the ratio of the return to strahl density across the event. The left-hand column of plots show the values as a function of time. The red portions in the lower three panels show when the spacecraft was in the solar wind. The right-hand column of plots are the corresponding PDF plots of the foreshock density only. The average foreshock and solar wind densities are shown to the right of each PDF plot (red solar wind, black foreshock). The beginning energy integration used to estimate the density in each region is shown at the top.
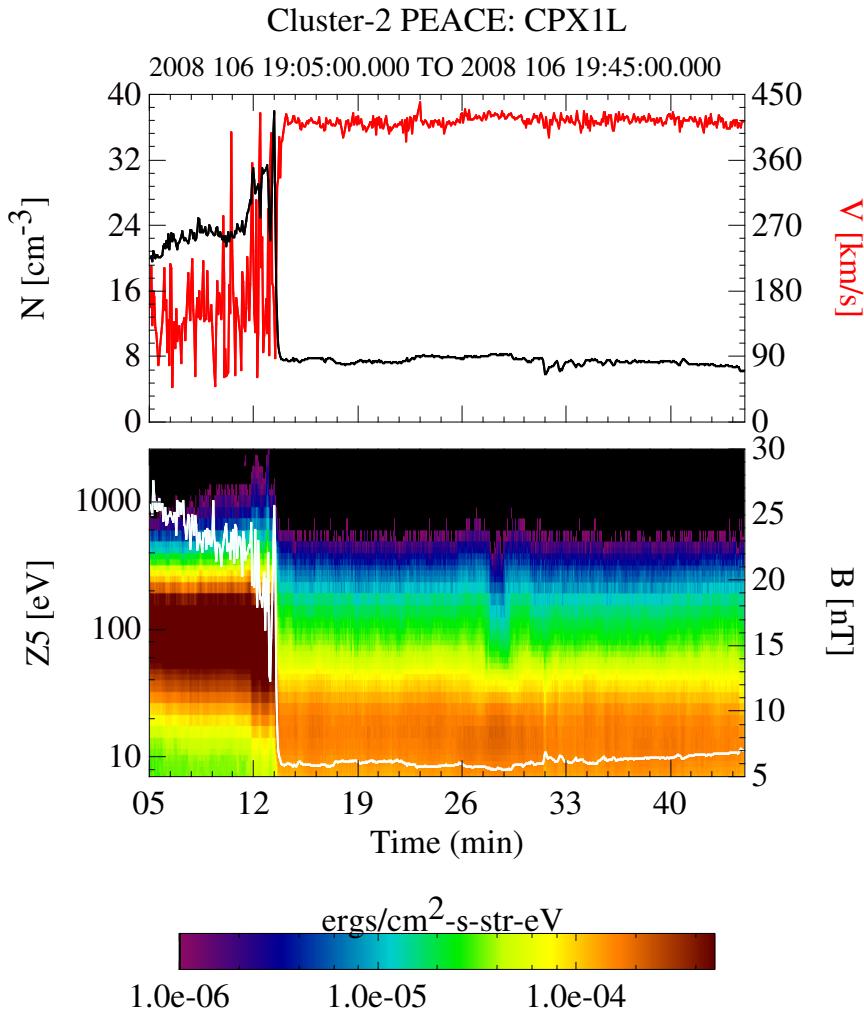
Fig. 11. An overview of the 2008-04-15 event. The lower panel shows an energy spectrogram of electron data from one of the near-ecliptic sensors of PEACE overlaid on a trace of the magnetic field (white). The upper panel contains the full electron density (black) and the bulk fluid velocity (red). All data were acquired from C2. At about 09:15 UT the spacecraft exits the magnetosheath, passes through the bow shock, and enters the upstream region and is in the foreshock for the remaining time period, with the exception of a brief excursion into the solar wind at about 19:28 UT.
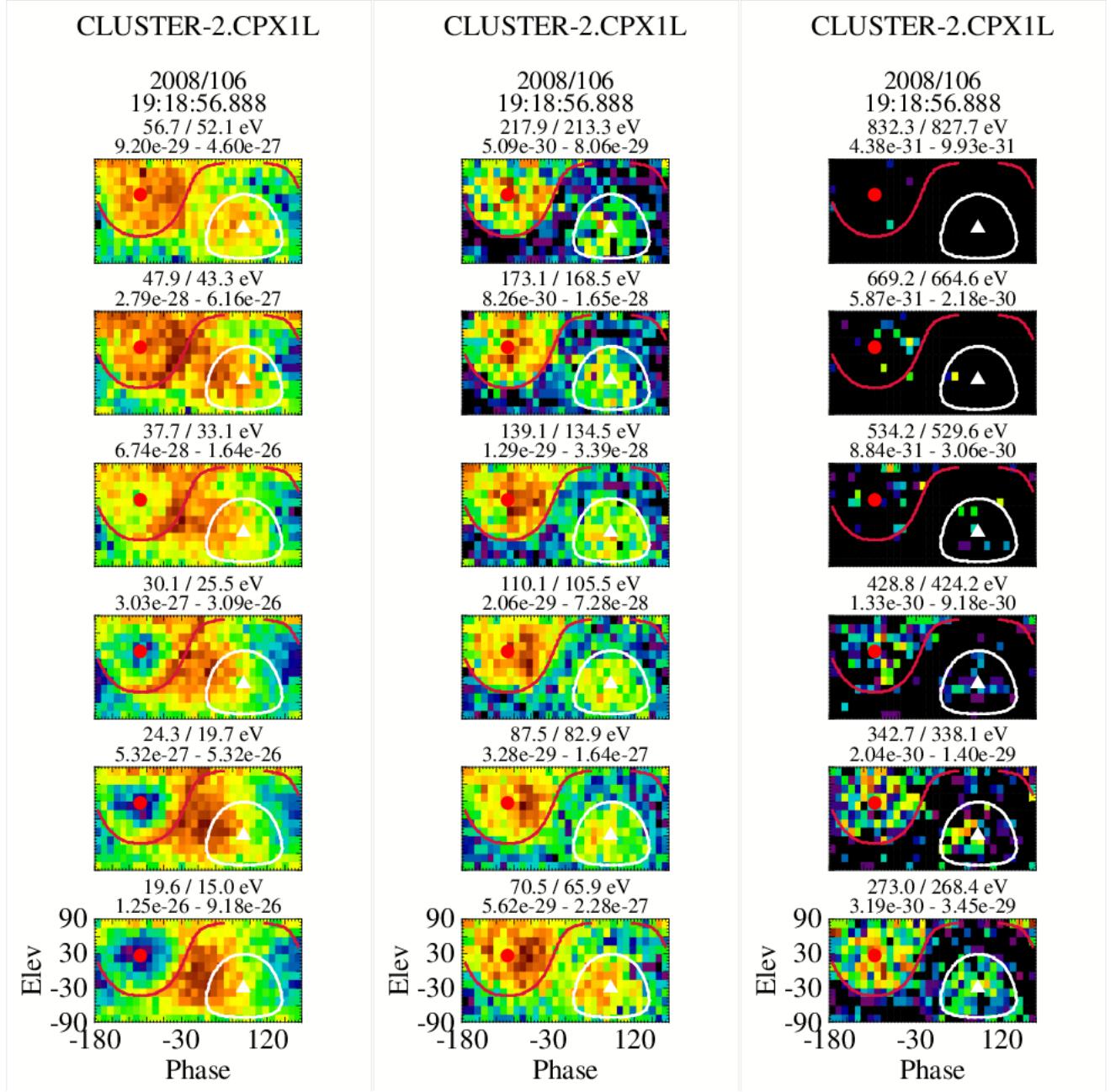
Fig. 12. A set of $\phi - \theta$ plots showing each energy step from 15.8 to 669.2 eV from a single eVDF in the foreshock. The white and red traces are lines of constant pitch-angle (125 and 70 degrees respectively) and are shown solely to indicate the areas where the strahl (white) and return electrons (red) might be expected to be found. The presence of either population may not exist at any given energy. The solid triangle and dot in the plots are the projections of the tail and head of the magnetic field vector respectively.
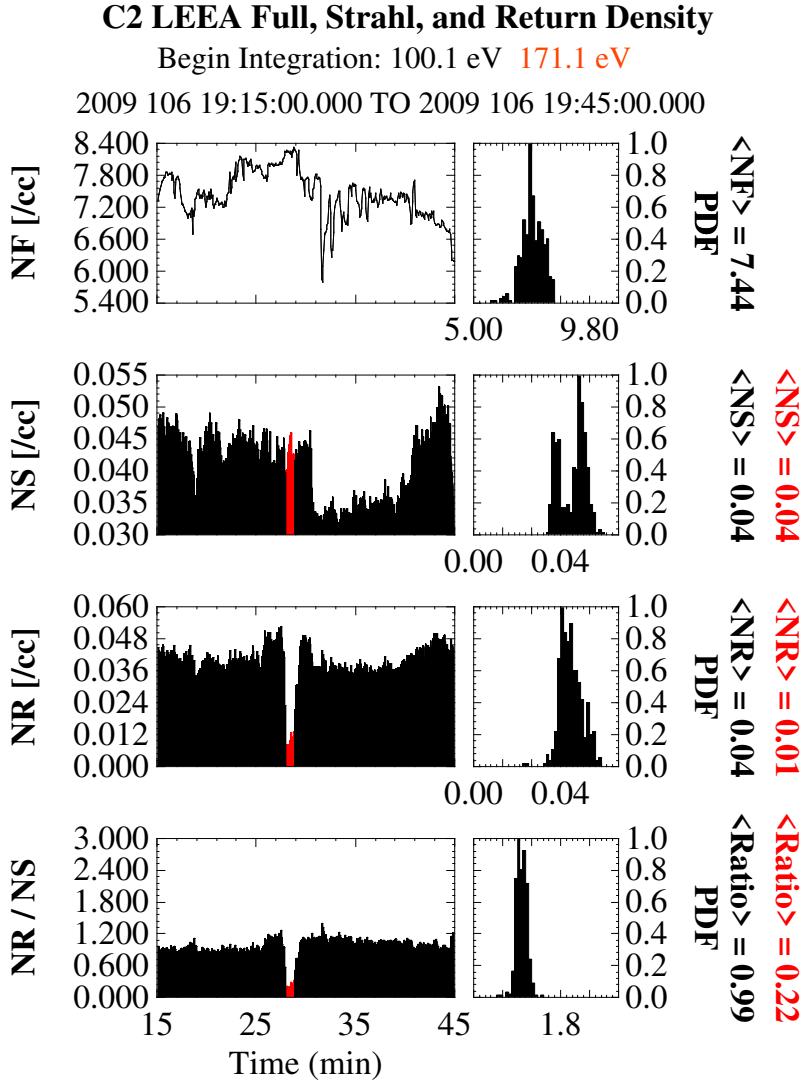
Fig. 13. Electron density information across the 2008-04-15 event. From top to bottom, the total, strahl and return electron densities and the ratio of the return to strahl density across the event. The left-hand column of plots show the values as a function of time. The red portions in the lower three panels show when the spacecraft was in the solar wind. The right-hand column of plots are the corresponding PDF plots of the foreshock density only. The average foreshock and solar wind densities are shown to the right of each PDF plot (red solar wind, black foreshock). The beginning energy integration used to estimate the density in each region is shown at the top.
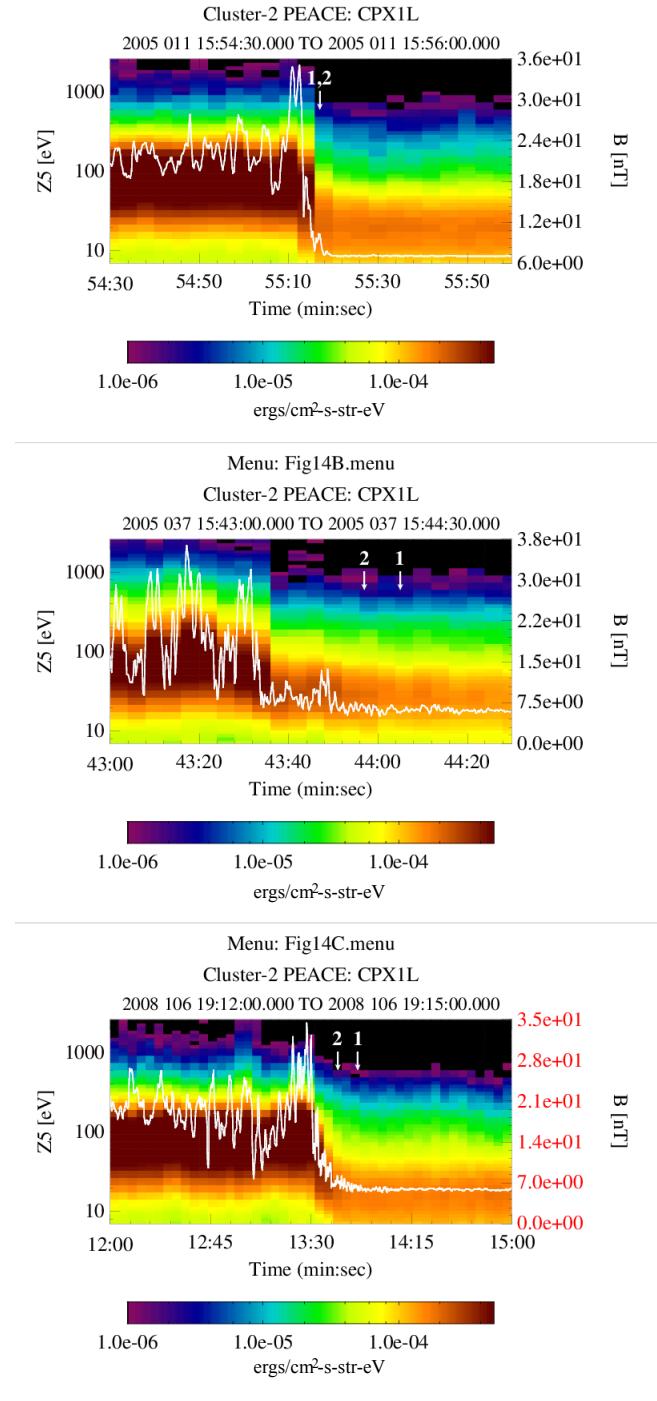
Fig. 14. High-resolution plots of the shock crossings for each of the three events. Each plot contains a spectrogram of the PEACE elevation Zone 5 sensor overlaid by the magnetic field. The spectrogram has a one spin resolution and the magnetic field resolution is 0.2s. There are two numbered arrows in each plot. Arrow 1 is the point at which the strahl disappears from the $\phi - \theta$ plots and arrow 2 where the return electron signature disappears. The location of the arrows is somewhat subjective, especially for arrow 2.

CLUSTERII.CLUSTER-2.CPX1L
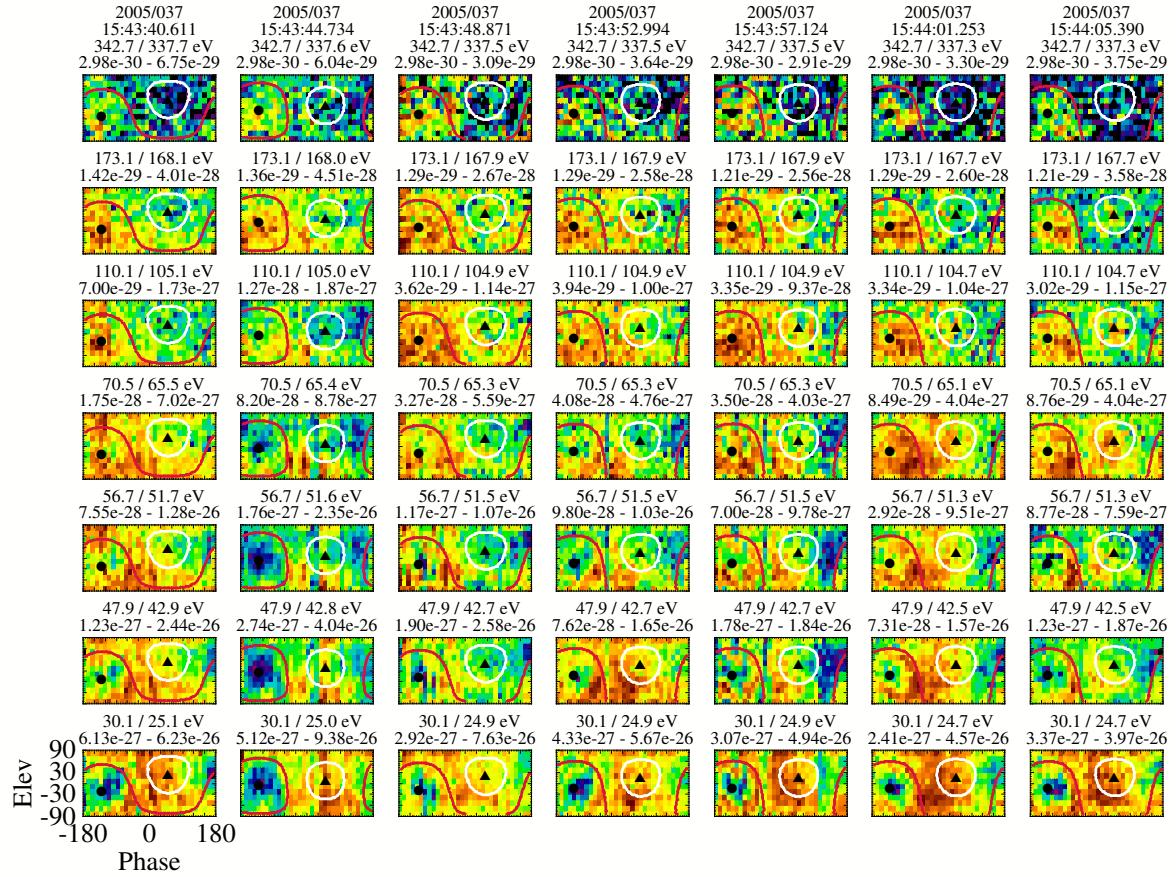
Fig. 15. Characteristics of 7 sequential eVDFs shown through $\phi - \theta$ plots which span the arrows shown in the center plot of Figure 14. Recall that the location of the strahl, when present, is expected within the white circle while the return electrons are expected within the red circle .